

## TOPICAL REVIEW

# Non-thermal atmospheric pressure discharges

A Fridman, A Chirokov and A Gutsol

Department of Mechanical Engineering, Drexel University, Philadelphia, PA, USA

Received 2 July 2003, in final form 9 November 2004

Published 6 January 2005

Online at [stacks.iop.org/JPhysD/38/R1](http://stacks.iop.org/JPhysD/38/R1)

## Abstract

There has been considerable interest in non-thermal atmospheric pressure discharges over the past decade due to the increased number of industrial applications. Diverse applications demand a solid physical and chemical understanding of the operational principals of such discharges. This paper focuses on the four most important and widely used varieties of non-thermal discharges: corona, dielectric barrier, gliding arc and spark discharge. The physics of these discharges is closely related to the breakdown phenomena. The main players in electrical breakdown of gases: avalanches and streamers are also discussed in this paper. Although non-thermal atmospheric pressure discharges have been intensively studied for the past century, a clear physical picture of these discharges is yet to be obtained.

## 1. Introduction

All varieties of plasma-chemical systems are traditionally divided into two major categories: thermal and non-thermal ones, characterized by their specific advantages and disadvantages. Thermal plasmas (usually arcs or radio frequency (RF) inductively coupled plasma discharges) are associated with Joule heating and thermal ionization, and enable the delivery of high power (to over 50 MW per unit) at high operating pressures. However, low excitation selectivity, very high gas temperature, serious quenching requirements and electrode problems result in limited energy efficiency and applicability of thermal plasma sources. Non-thermal plasmas (of low pressure glow, RF and microwave discharges) offer high selectivity and energy efficiency in plasma chemical reactions; they are able to operate effectively at low temperatures and without any special quenching.

So far non-thermal atmospheric pressure plasmas have been studied for a variety of industrial applications such as pollution control applications, volatile organic compounds (VOCs) removal, car exhaust emission control and polymer surface treatment (to promote wettability, printability and adhesion). For decades, non-thermal plasmas have been used to generate ozone for water purification.

Non-thermal plasmas may be produced by a variety of electrical discharges or electron beams. The basic feature of these various technologies is that they produce plasmas in which the majority of the electrical energy primarily goes into the production of energetic electrons—instead of heating the entire gas stream. These energetic electrons produce excited species—free radicals, and ions—as well as additional electrons through electron-impact dissociation, excitation and ionization of background gas molecules. These excited species, in turn, oxidize, reduce or decompose the pollutant molecules in pollution control applications. This is in contrast to the mechanism involved in thermal incineration processes (such as plasma-torches or furnaces and several chemical techniques), which require heating the entire gas stream in order to destroy the pollutants (for instance). In addition, low-temperature plasma technologies are highly selective and have relatively low maintenance requirements resulting in relatively low energy costs.

In this paper, first, we discuss in detail the theory of breakdown phenomena leading to the formation of different non-thermal plasma discharges and finally elucidate the physics and main features behind the major discharges intensively used in cutting-edge technologies. Together with well-known materials, the most interesting and important innovations in the area of non-thermal atmospheric pressure plasmas are also listed and discussed here.

## 2. Townsend and spark breakdown mechanisms

### 2.1. The Townsend mechanism of electric breakdown of gases

Electric breakdown is a complicated process of the formation of a conductive gas channel, which occurs when the electric field exceeds some critical value. As the result of the breakdown different kinds of plasmas are generated. Although breakdown mechanisms can be very sophisticated, all of them usually start with the electron avalanche. Electron avalanche is the multiplication of some primary electrons in cascade ionization.

Let us consider first the simplest breakdown in a plane gap of length  $d$  between electrodes connected to a dc power supply (with voltage  $V$ ), which provides the homogeneous electric field  $E = V/d$ . We can imagine some occasional formation of primary electrons near the cathode providing a very low initial current  $i_0$ . Each primary electron drifts to the anode, ionizing the gas (producing secondary electrons) and thus generates an avalanche. The avalanche develops both in time and in space, because the multiplication of electrons proceeds along with their drift from the cathode to anode (see figure 1). It is convenient to describe the ionization in the avalanche not by the ionization rate coefficient, but by the Townsend ionization coefficient  $\alpha$ , which gives the electron production per unit length or the multiplication of electrons (initial density  $n_{e0}$ ) per unit length along the electric field:  $dn_e/dx = \alpha n_e$  or equivalently  $n_e(x) = n_{e0} \exp(\alpha x)$ . The Townsend ionization coefficient is related to the ionization rate coefficient  $k_i(E/n_0)$  and electron drift velocity  $v_d$  as:

$$\alpha = \frac{v_i}{v_d} = \frac{1}{v_d} k_i \left( \frac{E}{n_0} \right) n_0 = \frac{1}{\mu_e} \frac{k_i(E/n_0)}{E/n_0}, \quad (1)$$

where  $v_i$  is the ionization frequency with respect to one electron and  $\mu_e$  is the electron mobility. Taking into account that breakdown starts at room temperature and the electron mobility is inversely proportional to pressure, it is convenient to write the Townsend coefficient  $\alpha$  as the similarity parameter  $\alpha/n_0$  depending on the reduced electric field  $E/n_0$ .

According to the definition of the Townsend coefficient  $\alpha$ , each primary electron generated near the cathode produces

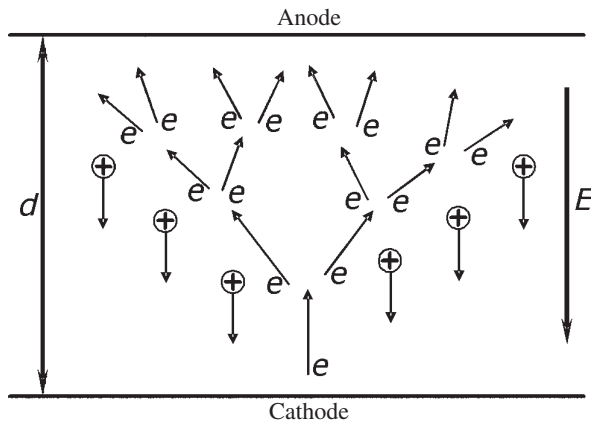


Figure 1. Illustration of the Townsend breakdown gap.

$\exp(\alpha d) - 1$  positive ions in the gap (see figure 1). We neglected the electron losses here due to recombination and attachment to electronegative molecules. Electron-ion recombination was neglected because the ionization degree is very low during the breakdown; attachment processes important in electronegative gases will be especially discussed below.

All the  $\exp(\alpha d) - 1$  positive ions produced in the gap per electron move back to the cathode, and altogether knock out  $\gamma[\exp(\alpha d) - 1]$  electrons from the cathode in the process of secondary electron emission, where  $\gamma$  is the secondary emission coefficient (third Townsend coefficient), defined as the probability of a secondary electron generation on the cathode by an ion impact. Obviously, the secondary electron emission coefficient  $\gamma$  depends on the cathode material, the state of the surface, type of gas and reduced electric field  $E/n_0$  (defining the ion energy). The typical value of  $\gamma$  in electric discharges is 0.01–0.1; the effect of photons and metastable atoms and molecules (produced in the avalanche) on the secondary electron emission is usually incorporated in the same ‘effective’  $\gamma$  coefficient.

The current in the gap is non-self-sustained as long as  $\gamma[\exp(\alpha d) - 1]$  is less than one, because positive ions generated by electron avalanche must produce at least one electron to start a new avalanche. As soon as the electric field, and hence the Townsend  $\alpha$  coefficient, becomes high enough the transition to self-sustained current (the breakdown!) takes place. Thus, the simplest breakdown condition in the gap can be expressed as

$$\gamma[\exp(\alpha d) - 1] = 1, \quad \alpha d = \ln \left( \frac{1}{\gamma} + 1 \right). \quad (2)$$

The Townsend breakdown mechanism is a mechanism of ignition of a self-sustained discharge in a gap, controlled by secondary electron emission from the cathode.

### 2.2. The critical electric field of Townsend breakdown

It is possible to derive relations for the breakdown electric field based on condition (2), by rewriting the expression (1) for the Townsend coefficient  $\alpha$  in the following conventional semi-empirical way, relating the similarity parameters  $\alpha/p$  and  $E/p$ , and also proposed initially by Townsend:

$$\frac{\alpha}{p} = A \exp \left( -\frac{B}{E/p} \right). \quad (3)$$

The parameters  $A$  and  $B$  of the relation (3) for numerical calculations of  $\alpha$  in different gases at  $E/p = 30$ – $500 \text{ V cm}^{-1} \text{ Torr}^{-1}$ , are given in table 1.

Combination of the relations (2) and (3) gives the following convenient formula for the calculation of the breakdown reduced electric field as a function of an important similarity parameter  $pd$ :

$$\frac{E}{p} = \frac{B}{C + \ln(pd)}. \quad (4)$$

In this relation the parameter  $B$  is the same as that in (3) and table 1. The parameter  $A$  is replaced by another one,  $C = \ln A - \ln[\ln(1/\gamma + 1)]$ .

**Table 1.** Numerical parameters  $A$  and  $B$  for calculation of the Townsend coefficient  $\alpha$ .

Gas	$A$ (cm <sup>-1</sup> Torr <sup>-1</sup> )	$B$ (V cm <sup>-1</sup> Torr <sup>-1</sup> )	Gas	$A$ (cm <sup>-1</sup> Torr <sup>-1</sup> )	$B$ (V cm <sup>-1</sup> Torr <sup>-1</sup> )
Air	15	365	N <sub>2</sub>	10	310
CO <sub>2</sub>	20	466	H <sub>2</sub> O	13	290
H <sub>2</sub>	5	130	He	3	34
Ne	4	100	Ar	12	180
Kr	17	240	Xe	26	350

The breakdown electric field dependence on the similarity parameter  $pd$ , which is described by relation (4), is usually referred to as the Paschen curve. The experimental Paschen curves for different gases are presented in Raizer's book [1]. These curves have a minimum voltage point, corresponding to the easiest breakdown conditions, which can be found from (4):

$$V_{\min} = \frac{eB}{A} \ln \left( 1 + \frac{1}{\gamma} \right), \quad \left( \frac{E}{p} \right)_{\min} = B, \quad (5)$$

$$(pd)_{\min} = \frac{e}{A} \ln \left( 1 + \frac{1}{\gamma} \right),$$

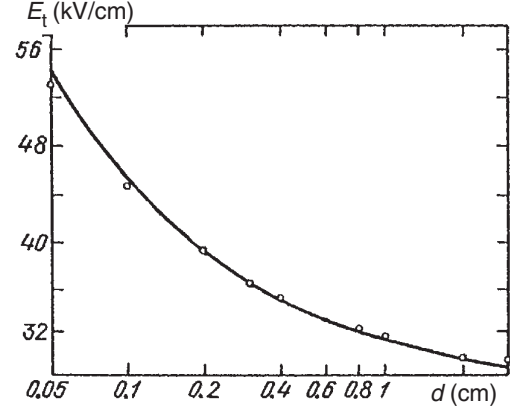
where  $e \approx 2.72$  is the base of natural logarithms.

The typical value of the minimum voltage necessary for breakdown is about 300 V, corresponding to a reduced electric field of about 300 V cm<sup>-1</sup> Torr<sup>-1</sup>. The right-hand branch of the Paschen curve (pressure more than 1 Torr for a gap of about 1 cm) is related to the case when the electron avalanche has enough distance and gas pressure to provide intensive ionization even at electric fields that are not very high. In this case, the reduced electric field is almost fixed and just slowly—logarithmically—reduces with  $pd$ -growth. The left-hand branch of the Paschen curve is related to the case when ionization is limited by the avalanche size and gas pressure. The ionization rate sufficient for breakdown can be provided in such a situation only by very high electric fields.

The reduced electric field at the Paschen minimum  $(E/p)_{\min} = B$  corresponds to the Stoletov constant, which is the minimum price of ionization (the minimum discharge energy necessary to produce one electron–ion pair). The price of ionization can be expressed in the case under consideration as  $W = eE/\alpha$  ( $e$  is the charge of an electron here), and its minimum, which is the Stoletov constant, is equal to  $W_{\min} = 2.72eB/A$ . The Stoletov constant usually exceeds the ionization potentials by several times because electrons use up their energy not only in ionization but also in vibrational and electronic excitation. The typical numerical estimate for the minimum ionization price in electric discharges with high electron temperatures is about 30 eV. It is interesting to note that the reduced electric field at the Paschen minimum (5) does not depend on  $\gamma$  and, hence, on cathode material in contrast to the minimum voltage  $V_{\min}$  and the corresponding similarity parameter  $(pd)_{\min}$ .

### 2.3. The Townsend breakdown mechanism in large gaps

The above-discussed Townsend mechanism of breakdown, which is relatively homogeneous and includes the development of independent avalanches, takes place usually at  $pd < 4000$  Torr cm (at atmospheric pressure  $d < 5$  cm). In larger gaps (more than 6 cm at atmospheric pressure) the avalanches

**Figure 2.** Breakdown electric field in atmospheric air [1].

essentially disturb the electric field and are no longer independent. It leads to the spark mechanism of breakdown, which we will discuss later on. Here, we will discuss gaps that are relatively large, but still not large enough for sparks.

The reduced electric field  $E/p$  necessary for breakdown (5) reduces logarithmically with  $pd$ . It is illustrated by the  $E(d)$  dependence in atmospheric air, presented in figure 2. The larger the gap and the avalanche, the less sensitive is the reduced electric field  $E/p$  to the secondary electron emission and cathode material. This explains the  $E/p$  reduction with  $pd$ .

This reduction in electronegative gases is limited, however, by the electron attachment processes. The influence of the attachment processes can be taken into account in a way similar to ionization by introducing the second Townsend coefficient  $\beta$ :

$$\beta = \frac{v_a}{v_d} = \frac{1}{v_d} k_a \left( \frac{E}{n_0} \right) n_0 = \frac{1}{\mu_e} \frac{k_a(E/n_0)}{E/n_0}. \quad (6)$$

In this relation  $k_a(E/n_0)$  and  $v_a$  are the attachment rate coefficient and attachment frequency with respect to an electron. The Townsend coefficient  $\beta$  gives the electron losses due to attachment per unit length. The combination of  $\alpha$  and  $\beta$  gives

$$\frac{dn_e}{dx} = (\alpha - \beta)n_e \quad \text{and} \quad n_e(x) = n_{e0} \exp[(\alpha - \beta)x]. \quad (7)$$

The Townsend coefficient  $\beta$  in the same way as  $\alpha$  is an exponential function of the reduced electric field. But ionization usually much exceeds attachment at relatively high values of the reduced electric fields, and the  $\beta$  coefficient can be neglected with respect to  $\alpha$  in this case (short gaps, relation (4)).

**Table 2.** Electric fields sufficient for the Townsend breakdown of centimetre-sized gaps at atmospheric pressure.

Gas	$E/p$ (kV cm <sup>-1</sup> )	Gas	$E/p$ (kV cm <sup>-1</sup> )	Gas	$E/p$ (kV cm <sup>-1</sup> )
Air	32	O <sub>2</sub>	30	N <sub>2</sub>	35
H <sub>2</sub>	20	Cl <sub>2</sub>	76	CCl <sub>2</sub> F <sub>2</sub>	76
CSF <sub>8</sub>	150	CCl <sub>4</sub>	180	SF <sub>6</sub>	89
He	10	Ne	1.4	Ar	2.7

This explains the absence of  $\beta$ -coefficients in the formulae in the previous section.

When the gaps are relatively large (in the range of centimetres at atmospheric pressure), the Townsend breakdown electric field in electronegative gases actually becomes constant and limited by the attachment processes. In this case, obviously, breakdown of electronegative gases requires much higher values of the reduced electric fields. The breakdown electric fields at high pressures for both electronegative and non-electronegative gases are presented in table 2.

The Townsend mechanism of breakdown was discussed above in the most general situations. Discussion of specific breakdown mechanisms such as electric breakdown in microwave, RF and low frequency fields, optical breakdown and breakdown of vacuum gaps is beyond the scope of this review but can be found, for example, in [1].

#### 2.4. The spark breakdown mechanism

Another breakdown mechanism, the so-called spark mechanism, takes place in large gaps at high pressures ( $d > 5$  cm at 1 atm). The sparks, in contrast to the Townsend mechanism, provide breakdown in the local narrow channel, without direct relation to electrode phenomena and with very high currents (up to  $10^4$ – $10^5$  A) and current densities.

The spark breakdown, as well as the Townsend breakdown, is primarily related to the avalanches, but in large gaps they cannot be considered as independent and stimulated by electron emission from the cathode. The spark breakdown at high  $pd$  develops much faster than the time necessary for ions to cross the gap and provide the secondary emission. Thus, the breakdown voltage in this case is independent of the cathode material, which is also evidence for the qualitative difference between the Townsend and spark mechanisms of breakdown.

The mechanism of spark breakdown is based on the concept of a streamer—a thin ionized channel, growing fast between electrodes; the concept of streamers was originally developed by Raether [2], Loeb [3] and Meek and Craggs [4]. Streamers are produced by an intensive primary avalanche if the space charge of this avalanche is large enough to create an electric field with a strength comparable to the applied electric field. This condition of streamer formation is also known as the Meek condition [4]. The details of streamer formation and propagation mechanisms will be covered later in this paper.

If the distance between electrodes is more than a metre or even kilometres long, the individual streamers are not sufficient to provide the large-scale spark breakdown (e.g. in the case of lightning). In this case, the so-called leader is moving from one electrode to another. The leader is like a streamer in a

thin channel but much more conductive. The leader actually includes the streamers as its elements. Because all types of breakdown considered include the avalanche phase as an initial stage of breakdown development we give a detailed description of avalanche development in the next section.

#### 2.5. Electron avalanches

Adding to equation (7) similar equations ( $N_e$ ) for positive ( $N_+$ ) and negative ( $N_-$ ) ions we have a system of equations that describes an avalanche moving along the axis  $x$ :

$$\begin{aligned} \frac{dN_e}{dx} &= (\alpha - \beta)N_e, & \frac{dN_+}{dx} &= \alpha N_e, \\ \frac{dN_-}{dx} &= \beta N_e, \end{aligned} \quad (8)$$

where  $\alpha$  and  $\beta$  are the ionization and attachment Townsend coefficients. If the avalanche starts from the one primary electron, the numbers of charged particles—electrons, positive and negative ions—can be found from (8) as

$$\begin{aligned} N_e &= \exp[(\alpha - \beta)x], & N_+ &= \frac{\alpha}{\alpha - \beta}(N_e - 1), \\ N_- &= \frac{\beta}{\alpha - \beta}(N_e - 1). \end{aligned} \quad (9)$$

The electrons in the avalanche move in the direction of the non-disturbed electric field  $E_0$  (axis  $x$ ) with the drift velocity  $v_d = \mu_e E_0$ . At the same time, free diffusion ( $D_e$ ) makes the group of electrons spread around the axis  $x$  in the radial direction  $r$ . Taking into account both the drift and the diffusion, the electron density in the avalanche can be introduced in the following form [5]:

$$\begin{aligned} n_e(x, r, t) &= \frac{1}{(4\pi D_e t)^{3/2}} \exp \left[ -\frac{(x - \mu_e E_0 t)^2 + r^2}{4D_e t} \right. \\ &\quad \left. + (\alpha - \beta)\mu_e E_0 t \right]. \end{aligned} \quad (10)$$

The avalanche radius  $r_A$  (where the electron density is  $e$  times less than on the axis  $x$ ) grows with time and the distance  $x_0$  of the avalanche propagation, in accordance with the conventional diffusion relation, where we took into account the Einstein relation between the electron mobility and free diffusion coefficient.

$$r_A = \sqrt{4D_e t} = \sqrt{4D_e \frac{x_0}{\mu_e E_0}} = \sqrt{\frac{4T_e}{eE_0}} x_0. \quad (11)$$

Based on the expression for electron concentration (10), we can calculate the space distribution of positive and negative ion densities during the short interval of avalanche propagation, when the ions actually remain at rest:

$$\begin{aligned} n_+(x, r, t) &= \int_0^t \alpha \mu_0 E_0 n_e(x, r, t') dt', \\ n_-(x, r, t) &= \int_0^t \beta \mu_0 E_0 n_e(x, r, t') dt'. \end{aligned} \quad (12)$$

A simplified expression for the positive ion density space distribution not too far from the  $x$ -axis can be derived based

on relations (10) and (12) in the absence of attachment and in the limit  $t \rightarrow \infty$  [5] as

$$n_+(x, r) = \frac{\alpha}{\pi r_A^2(x)} \exp \left[ \alpha x - \frac{r^2}{r_A^2(x)} \right], \quad (13)$$

where  $r_A(x)$  is the avalanche radius. The ion concentration in the trail of the avalanche grows along the axis in accordance with the exponential increase (9) in the number of electrons.

Although the avalanche radius grows proportionally to  $x^{1/2}$ , the visible avalanche outline is wedge-shaped. This means that the visible avalanche radius is growing linearly (proportionally to  $x$ ). This happens because the visible avalanche radiation is determined by the absolute density of excited species, which is approximately proportional to the exponential factor  $\Phi$  in the expression (13) and, obviously, grows with  $x$ . The visible avalanche radius  $r(x)$  can then be written using the relation (13), taking into account the small value of  $r$  at small  $x$ , as:

$$\frac{r^2(x)}{r_A^2(x)} = \alpha x - \ln \Phi, \quad (14)$$

$$r(x) \approx r_A(x) \sqrt{\alpha x} = \sqrt{\frac{4T_e x}{eE_0}} * \alpha x = x \sqrt{\frac{4T_e \alpha}{eE_0}},$$

which explains the linearity of  $r(t)$  and the wedge shape of the avalanche.

The qualitative change in avalanche behaviour takes place when the charge amplification  $\exp(\alpha x)$  is high. In this case, the production of a space charge with its own significant electric field  $E_a$  takes place. This local electric field  $E_a$  should be added to the external field  $E_0$ . Because the electrons are much faster than ions the electrons always run at the head of the avalanche leaving the ions behind and thus creating a dipole with the characteristic length  $1/\alpha$  (distance that the electrons move before ionization) and charge  $N_e \approx \exp(\alpha x)$ .

The dipole formation provokes the appearance of the external electric field distortion. In front of the avalanche head (and behind the avalanche) the electric field has its maximum value (the sum of  $E_0$  and  $E_a$ ), which obviously accelerates ionization in these areas. Vice versa, inside the avalanche, the total electric field is lower than the external one, which slows down the ionization. Also, the space charge creates the radial electric field. The electric field of the charge  $N_e \approx \exp(\alpha x)$  at a distance of about the avalanche radius reaches the value of the external field  $E_0$  at some critical value of  $\alpha x$ .

Note, that when  $\alpha x \geq 14$  the radial growth of an avalanche due to repulsion drift of electrons exceeds the diffusion effect, and should be taken into account. In this case, the avalanche radius grows with  $x$  as:

$$r = \sqrt[3]{\frac{3e}{4\pi \epsilon_0 \alpha E_0}} \exp \frac{\alpha x}{3} = \frac{3}{\alpha} \frac{E_a}{E_0}. \quad (15)$$

This fast growth of the transverse avalanche size restricts the electron density in the avalanche to the maximum value

$$n_e = \frac{\epsilon_0 \alpha E_0}{e}. \quad (16)$$

When the transverse avalanche size reaches the characteristic ionization length  $1/\alpha \approx 0.1$  cm, the broadening

of the avalanche head slows down dramatically. Obviously, the avalanche electric field is roughly equal to the external one in this case (see equation (15)). Typical values of the maximum electron density in an avalanche are about  $10^{12}$ – $10^{13}$  cm $^{-3}$ .

When the avalanche head reaches the anode, the electrons sink into the electrode leaving the ions to occupy the discharge gap. In the absence of electrons, the total electric field is due to the external field, the ionic trail and also the ionic charge ‘image’ in the anode. The resulting electric field in the ionic trail near the anode is less than the external electric field, but farther away from the electrode it exceeds  $E_0$ . The total electric field reaches the maximum value on the characteristic ionization distance (about 0.1 cm from the anode).

## 2.6. The streamers

A strong primary avalanche amplifies the external electric field, leading to the formation of a thin weakly ionized plasma channel—the so-called streamer. When the streamer channel connects the electrodes, the current may be significantly increased to form the spark. The avalanche-to-streamer transformation takes place when the internal field of an avalanche becomes comparable with the external one, that is, when the amplification parameter  $\alpha d$  is large enough. At relatively small discharge gaps, the transformation occurs only when the avalanche reaches the anode. Such a streamer is known as the cathode-directed or positive streamer. If the discharge gap and overvoltage are large enough, the avalanche-to-streamer transformation can take place quite far from the anode. In this case, the so-called anode-directed or negative streamer is able to grow towards both the electrodes.

The cathode-directed streamer starts near the anode. It looks like and operates as a thin conductive needle growing from the anode. The electric field at the tip of the ‘anode needle’ is very high, which stimulates fast streamer propagation in the direction of the cathode. Usually, the streamer propagation is limited by neutralization of the ionic trail near the tip of the needle. The electric field there is so high, that it provides electron drift with a velocity of about  $10^8$  cm s $^{-1}$ .

The anode-directed streamer occurs between the electrodes, if the primary avalanche becomes strong enough even before reaching the anode. The streamer propagates in the direction of the cathode in the same way as the cathode-directed streamer. The mechanism of streamer growth in the direction of the anode is also similar, but in this case the electrons from the primary avalanche head neutralize the ionic trail of secondary avalanches. However, the secondary avalanches could be initiated here not only by photons, but also by some electrons moving in front of the primary avalanche.

## 2.7. The Meek criterion of streamer formation

The formation of a streamer requires the electric field of the space charge in the avalanche,  $E_a$ , to be of the order of the external field  $E_0$ :

$$E_a = \frac{e}{4\pi \epsilon_0 r_A^2} \exp \left[ \alpha \left( \frac{E_0}{p} \right) * x \right] \approx E_0. \quad (17)$$

Taking the avalanche head radius as the ionization length— $r_a \approx 1/\alpha$ —the criterion of streamer formation in the gap with the distance  $d$  between electrodes can be presented as the requirement for the avalanche amplification parameter  $\alpha d$  to exceed the critical value:

$$\alpha \left( \frac{E_0}{p} \right) * d = \ln \frac{4\pi\epsilon_0 E_0}{e\alpha^2} \approx 20, \quad (18)$$

$$N_e = \exp(\alpha d) \approx 3 \times 10^8.$$

This fundamental and important criterion of streamer formation is known as Meek's breakdown condition ( $\alpha d \geq 20$ ).

Electron attachment processes in electronegative gases slow down the electron multiplication in avalanches and increase the value of the electric field required for streamer formation. The situation here is similar to that in the Townsend breakdown mechanism. Actually, the ionization coefficient  $\alpha$  in Meek's breakdown condition should be replaced in electronegative gases by  $\alpha - \beta$ . However, practically, when the discharge gaps are not too large (in air  $d \leq 15$  cm), the electric fields required by the Meek criterion are relatively high; then,  $\alpha \gg \beta$  and the attachment can be neglected.

Increasing  $d$  in electronegative gases does not lead to a gradual decrease of the electric field necessary for streamer formation, but it is limited by some minimum level. The minimal electric field required for streamer formation can be found from the ionization–attachment balance:  $\alpha(E_0/p) = \beta(E_0/p)$ .

We should note that electric field non-uniformity has a strong influence on breakdown conditions and the avalanche transformation into a streamer. Quite obviously, the non-uniformity decreases the breakdown voltage for a given distance between the electrodes.

### 2.8. The streamer breakdown mechanism

Dawson and Winn [6] and Gallimberti [7] proposed a model of propagation of the quasi-self-sustained streamers. This model assumes very low conductivity of a streamer channel, which makes the streamer propagation autonomous and independent of the anode. Photons initiate avalanche at a distance  $x_1$  from the centre of the positive charge zone of radius  $r_0$ . According to the model, the avalanche then develops in the autonomous electric field of the positive space charge  $E(x) = eN_+/4\pi\epsilon_0 x^2$ , the number of electrons increases by ionization as:  $N_e = \int_{x_1}^{x_2} \alpha(E) dx$ , and the avalanche radius grows due to diffusion as:

$$\frac{dr^2}{dt} \approx 4D_e, \quad r(x_2) = \left[ \int_{x_1}^{x_2} \frac{4D_e}{\mu_e E(x)} dx \right]^{1/2}. \quad (19)$$

To provide continuous and steady propagation of the self-sustained streamer, its positive space charge  $N_+$  should be compensated by the negative charge of the avalanche head  $N_e = N_+$  at the meeting point of the avalanche and streamer:  $x_2 = r_0 + r$ . Also, the radii of the avalanche and streamer should be correlated at this point  $r = r_0$ . All these equations permit us to describe the streamer parameters including the propagation velocity, which is given by  $x_2$  divided by the time of the avalanche displacement from  $x_1$  to  $x_2$ . The model of the quasi-self-sustained streamer is helpful in the description

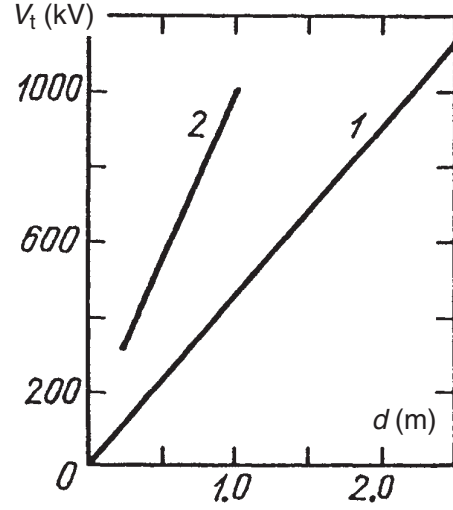


**Figure 3.** Breakdown voltage in air at 50 Hz: (1) rod–rod gap, (2) rod–plane gap.

of breakdown of long gaps with high voltage and low average electric fields (see figure 3).

Klingbeil *et al* [8] and Lozansky and Firsov [5] proposed a qualitatively different model of streamer propagation. In contrast to the above approach, this model considers the streamer channel as an ideal conductor connected to the anode. The ideally conducting streamer channel is considered in the framework of this model as an anode elongation in the direction of the external electric field  $E_0$  with the shape of an ellipsoid of revolution.

According to the approach that uses the ideally conducting streamer, the streamer propagation at each point of the ellipsoid is normal to its surface. The propagation velocity is equal to the electron drift velocity in the appropriate electric field. For the calculation of the streamer growth velocity a convenient formula for the maximum electric field  $E_m$  on the tip of the streamer with length  $l$  and radius  $r$  was proposed by Baselyan and Goryunov [9]:

$$\frac{E_m}{E_0} = 3 + \left( \frac{l}{r} \right)^{0.92}, \quad 10 < \frac{l}{r} < 2000. \quad (20)$$

The model of the ideally conducting streamer is in reasonably good agreement with experimental results.

### 2.9. The leader breakdown mechanism

As discussed above, three processes lead to the spark (or streamer) breakdown mechanism: avalanche to streamer transition; the streamer growth from the anode to the cathode; and the triggering of a return wave of intense ionization, which results in spark formation. This breakdown mechanism sequence is not valid for very long gaps—particularly in electronegative gases (including air). It happens because the streamer channel conductivity is not high enough to transfer the anode potential close to the cathode and stimulate there the return wave of intense ionization and spark. In electronegative gases where the streamer channel conductivity is lower this effect is especially strong. Also, in non-uniform electric fields, the streamer head grows from the strong to the weak

field region, which slows down its propagation and streamers just stop in the long air gaps without reaching the opposite electrode.

The breakdown of gaps with multi-metre and kilometre long inter-electrode distances, is related to the formation and propagation of the leaders. With respect to the streamer, the leader is highly ionized and there is a highly conductive plasma channel growing from the active electrode along the path prepared by the preceding streamers. The high conductivity of the leaders makes them more effective with respect to the streamers in transferring the anode potential close to the cathode and stimulating there the return wave of intense ionization and the spark. Lightning is the most common natural phenomenon associated with leaders.

The heating effect of the relatively short centimetre long streamers is about 10 K while for metre long channels it reaches 3000 K near the active electrode. This heating together with the corresponding high level of non-equilibrium excitation of atoms and molecules probably explains the transformation of a streamer channel into the leader. The temperature of 3000 K is not enough for sufficient thermal ionization of air, but this temperature together with the elevated non-equilibrium excitation level is high enough for other mechanisms of increase of electrical conductivity in the plasma channel.

Thus, Gallimberti [10] assumed the mechanism of streamer-to-leader transition in air related to thermal detachment of electrons from the negative ions of oxygen, which are the main products of electron attachment in the electronegative gas. The effective destruction of these negative ions, and as a result compensation of electron attachment, becomes possible if the temperature exceeds 1500 K in dry air and 2000 K in humid air. Such temperatures are available in the plasma channel and can provide the formation of the high conductivity leader in electronegative gas. Note, that during the evolution of a streamer in air, the Joule heat is stored at first in the vibrational excitation of  $N_2$  molecules. While the temperature of air is increasing, the VT-relaxation (VT—vibrational translational) grows exponentially providing the explosive heating of the plasma channel.

So far we have discussed only the general physical features and kinetics of charged species in avalanches, streamers and leaders. In the following sections we consider the role of the avalanches, streamers and leaders in the specific discharge systems—in particular in corona, spark and dielectric-barrier discharges (DBDs).

### 3. The corona discharge

#### 3.1. Overview of the corona discharge

The corona is a weakly luminous discharge, which usually appears at atmospheric pressure near sharp points, edges or thin wires where the electric field is sufficiently large. Thus, corona discharges are always non-uniform: strong electric field, ionization and luminosity are actually located in the vicinity of one electrode. Charged particles are dragged by the weak electric fields from one electrode to another to close the electric circuit. However, in the initial stages, the breakdown circuit in the corona discharge is closed by displacement current rather than charged particle transport [77]. A corona can be

observed in air around high voltage transmission lines, around lightning rods, and even masts of ships, where it is called ‘Saint Elmo’s fire’.

The corona discharge can be ignited with a relatively high voltage, which mainly occupies the region around one electrode. If the voltage grows even larger, the remaining part of the discharge gap breaks down and the corona transfers into the spark. Here, we present only the main physical and engineering principals of the continuous corona discharge; more details on the subject can be found in the publications of Loeb [11] and Goldman and Goldman [12].

#### 3.2. Negative and positive corona

The mechanism for sustaining the continuous ionization level in a corona depends on the polarity of the electrode where the high electric field is located. If the high electric field zone is located around the cathode, we call it a negative corona. If the high electric field is concentrated in the region of the anode, such a discharge is called a positive corona.

Continuity of electric current from the cathode into the plasma is provided by secondary emission from the cathode (mostly induced by ion impact). Ignition of the negative corona actually involves the same mechanism as the Townsend breakdown, obviously generalized by taking into account the non-uniformity and possible electron attachment processes:

$$\int_0^{x_{\max}} [\alpha(x) - \beta(x)] dx = \ln \left( 1 + \frac{1}{\gamma} \right). \quad (21)$$

In this equation,  $\alpha(x)$ ,  $\beta(x)$  and  $\gamma$  are the first, second and third Townsend coefficients, describing, respectively, ionization, electron attachment and secondary electron emission from the cathode;  $x_{\max}$  corresponds to the distance from the cathode, where the electric field becomes low enough and  $\alpha(x_{\max}) = \beta(x_{\max})$ , which means that no additional electron multiplication takes place. The equality  $\alpha(x_{\max}) = \beta(x_{\max})$  actually corresponds to the breakdown electric field  $E_{\text{break}}$  in electronegative gases. If the gas is not electronegative ( $\beta = 0$ ), integration of equation (21) is formally not limited; however, due to the exponential decrease of  $\alpha(x)$  an effective  $x_{\max}$  can be chosen.

Note that the critical distance  $x = x_{\max}$  determines not only the ionization, but also the electronic excitation zone, and hence the zone of plasma luminosity. This means that the critical distance  $x = x_{\max}$  can be considered as the visible size of the corona.

Ionization in the positive corona cannot be provided by the cathode phenomenon due to the low electric field in the cathode region. Here, ionization processes are related to the formation of the cathode-directed streamers. Ignition conditions can be described for the positive corona using the criteria of cathode-directed streamer formation. In this case, a generalization of Meek’s breakdown criterion, equation (18), is quite a good approximation, taking into account the non-uniformity of the corona and possible contributions of electron attachment:

$$\int_0^{x_{\max}} [\alpha(x) - \beta(x)] dx \approx 18\text{--}20. \quad (22)$$

In comparison with similar ignition criteria given by equation (21), the minimal values of the amplification

coefficients should be 2–3 times lower to provide ignition of a negative corona (because  $\ln(1/\gamma) \approx 6-8$ ). However, the critical values of the electric field for ignition of positive and negative coronas are very close, even though these are related to very different breakdown mechanisms. Also, it was shown that the critical values of the electric field for negative corona ignition do not depend on electrode composition as they should according to the Townsend breakdown mechanism [69]. This can be explained by the strong exponential dependence of the amplification coefficients on the electric field value. Another possible explanation is related to the contribution of indirect ionization processes, such as metastable–metastable collisions, to the amplification coefficients [69].

### 3.3. Ignition criterion for corona in air

According to equations (21) and (22), ignition for both positive and negative coronas is mostly determined by the value of the maximum electric field in the vicinity of the electrode where the discharge is to be initiated. The critical value of the igniting electric field for the case of coaxial electrodes in air can be calculated numerically using the empirical Peek formula:

$$E_{cr} \left( \frac{\text{kV}}{\text{cm}} \right) = 31\delta \left( 1 + \frac{0.308}{\sqrt{\delta r(\text{cm})}} \right), \quad (23)$$

where  $\delta$  is the ratio of air density to the standard value and  $r$  is the radius of the internal electrode. The formula can be applied for pressures 0.1–10 atm, polished internal electrodes with radius  $r \approx 0.01-1$  cm, with both dc and ac with frequencies up to 1 kHz. If the electrodes are rough, the critical electric field decreases by 10–20%.

Although the Peek formula was derived for the case of coaxial cylinders, it can be used for other corona configurations also, with slightly different values of coefficients. As an example, the critical corona-initiating electric field in the case of two parallel wires can be calculated using the following empirical formula:

$$E_{cr} \left( \frac{\text{kV}}{\text{cm}} \right) = 30\delta \left( 1 + \frac{0.301}{\sqrt{\delta r(\text{cm})}} \right). \quad (24)$$

Both relations (23) and (24) correspond to simplified empirical formulae for the Townsend coefficient  $\alpha$  in air at reduced electric fields  $E/p < 150 \text{ V cm}^{-1} \text{ Torr}^{-1}$ :

$$\alpha \text{ (cm}^{-1}\text{)} = 0.14 \times \delta \left[ \left( \frac{E(\text{kV cm}^{-1})}{31\delta} \right)^2 - 1 \right]. \quad (25)$$

Equations (23) and (24) determine the critical value of the corona electric field. The critical value of the electric field is supposed to be reached in the close vicinity of an active electrode.

### 3.4. Active corona volume

The ionization of charged particles takes place in corona discharges only in the vicinity of an electrode where the electric field is sufficiently high. This zone is usually referred to as the active corona volume (see figure 4). From the point of view of

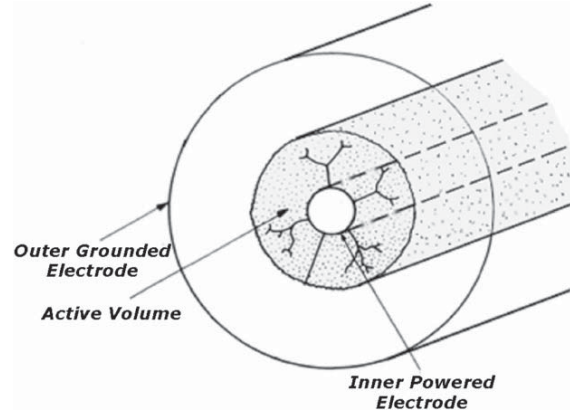


Figure 4. Illustration of active corona volume.

plasma-chemical applications the active corona volume is the most important part of the discharge, because most excitation and reaction processes take place in this zone. The external radius of the active corona volume is determined by the value of the electric field corresponding to the breakdown value  $E_{\text{break}}$  on the boundary of the active volume.

The minimum value of voltage required for corona ignition in air (at normal conditions), between a thin wire electrode of radius  $r = 0.1$  cm and coaxial cylinder external electrode with radius  $R = 10$  cm, is about 30 kV. At the same time, the electric field near the external electrode is relatively very low  $E(R) \approx 0.6 \text{ kV cm}^{-1}$ ,  $E(R)/p \approx 0.8 \text{ V cm}^{-1} \text{ Torr}^{-1}$ , and obviously not sufficient for ionization. Effective multiplication of charges requires the breakdown of the electric field, which can be estimated as  $E_{\text{break}} \approx 25 \text{ kV cm}^{-1}$ . This determines the external radius of the active corona volume case as  $r_{\text{AC}} = r E_{\text{cr}}/E_{\text{break}} \approx 0.25$  cm. Hence, the active corona volume occupies the cylindrical layer  $0.1 \text{ cm} < x < 0.25$  cm around the thin wire.

In general, the external radius of the active corona volume around the thin wire can be determined as

$$r_{\text{AC}} = \frac{V}{E_{\text{break}} \ln(R/r)}, \quad (26)$$

where  $V$  is the voltage applied to sustain the corona discharge. As can be seen from equation (26), the radius of the active corona volume increases with applied voltage.

Similar to equation (26), the external radius of the active corona volume generated around a sharp point can be expressed as

$$r_{\text{AC}} \approx \sqrt{\frac{rV}{E_{\text{break}}}}. \quad (27)$$

Based on equations (26) and (27), compare the active radii of the corona around a thin wire and a sharp point:

$$\frac{r_{\text{AC}}(\text{wire})}{r_{\text{AC}}(\text{point})} \approx \frac{1}{\ln(R/r)} \sqrt{\frac{V}{aE_{\text{break}}}} = \frac{r_{\text{AC}}(\text{point})}{r \ln(R/r)}. \quad (28)$$

Numerically, this ratio is typically about 3, which illustrates the advantage of a corona generated around a thin wire, to produce a larger volume of non-thermal atmospheric pressure plasma effective for different applications.

### 3.5. Influence of the space charge on the electric field in corona discharges

Charged particles are produced only in the active corona volume in the vicinity of an electrode. Thus, the electric current to the external electrode outside the active volume is provided by the drift of charged particles (generated in the active volume) in the relatively low electric field. In the positive corona these drifting particles are positive ions, and in the negative corona, negative ions (or electrons, if the corona is generated in non-electronegative gas mixtures).

The discharge current is determined by the difference between the applied voltage  $V$  and the critical one  $V_{cr}$ , corresponding to the critical electric field  $E_{cr}$ , and its value is limited by the space charge outside the active corona volume. The current of charged particles is partially reflected back by the space charge formed by these particles. The phenomenon is somewhat similar to the phenomenon of current limitation by space charge in sheaths, or in vacuum diodes. However, in the case under consideration, the motion of charged particles is not collisionless, but determined by the drift in electric field.

The electric current per unit length of the wire  $i$  in the corona generated between coaxial cylinders with radii  $R$  and  $r$  is constant outside the active corona volume (where there is no charge multiplication):

$$i = 2\pi x en \mu E = \text{const.} \quad (29)$$

Here,  $x$  is the distance from the corona axis,  $n$  the number density of charged particles providing electrical conductivity outside the active volume and  $\mu$  is the mobility of the charged particles. Assuming that the space charge perturbation of the electric field is not very strong, the number density distribution  $n(x)$  can be found, to a first approximation, based on equation (29) and the non-perturbed electric field distribution:

$$n(x) = \frac{i}{2\pi e \mu E x} = \frac{i \ln(R/r)}{2\pi e \mu V} = \text{const.} \quad (30)$$

Using Maxwell's equations for the case of cylindrical symmetry and expression (30) one can find the second approximation of the electric field distribution  $E(x)$ :

$$\begin{aligned} \frac{1}{x} \frac{d[xE(x)]}{dx} &= \frac{1}{\varepsilon_0} en(x), \\ \frac{1}{x} \frac{d[xE(x)]}{dx} &= \frac{i \ln(R/r)}{2\pi \varepsilon_0 \mu V}. \end{aligned} \quad (31)$$

Integration of Maxwell's equation yields the electric field distribution, which takes into account the current and, hence, the space charge:

$$E(x) = \frac{V_{cr} \ln(R/r)}{x} + \frac{i \ln(R/r)}{2\pi \varepsilon_0 \mu V} \frac{x^2 - r^2}{2x}. \quad (32)$$

Also, equation (32) is valid only in the case of small electric field perturbations due to the space charge outside the active corona volume. Expressions similar to equation (32), describing the influence of electric current and space charge on the electric field distribution, can be derived for other corona configurations (see Roth [13]).

### 3.6. Current–voltage characteristics of a corona discharge

Integration of the expression (32) over the radius  $x$  taking into account that in most of the corona discharge gap  $x^2 \gg r^2$ , gives the relation between current (per unit length) and voltage of the discharge, which is the current–voltage characteristic of the corona generated around a thin wire:

$$i = \frac{4\pi \varepsilon_0 \mu V (V - V_{cr})}{R^2 \ln(R/r)}. \quad (33)$$

From this equation, it follows that the corona current depends on the mobility of the main charged particles providing conductivity outside the active corona volume. Noting that the mobilities of positive and negative ions are nearly equal, the electric currents in positive and negative corona discharges are also similar. A negative corona in gases without electron attachment (e.g. noble gases) provides much larger currents because electrons are able to rapidly leave the discharge gap without forming a significant space charge. Even a small admixture of an electronegative gas decreases the corona current.

It is important to note that the parabolic current–voltage characteristic equation (33) is valid not only for thin wires, but for other corona configurations. Thus, the coefficients before the quadratic form  $V(V - V_{cr})$  are different for different geometries of corona discharges ( $I$  is the total current in the corona discharge):

$$I = CV(V - V_{cr}). \quad (34)$$

The current–voltage characteristic for the corona generated in atmospheric air between a sharp point cathode with radius  $r = 3\text{--}50 \mu\text{m}$  and a perpendicular flat anode located at a distance of  $d = 4\text{--}16 \text{ mm}$  can be expressed as

$$I (\mu\text{A}) = \frac{52}{(d \text{ (mm)})^2} (V \text{ (kV)})(V - V_{cr}). \quad (35)$$

In this empirical relation  $I$  is the total corona current from the sharp point cathode. The critical corona ignition voltage  $V_{cr}$  in this case can be taken as 2.3 kV and does not depend on the distance  $d$  [12].

### 3.7. Power released in the continuous corona discharge

Based on the current–voltage characteristic equation (33), the electric power released in the continuous corona discharge can be determined for the case of a long thin wire of length  $L$  as

$$P = \frac{4\pi L \varepsilon_0 \mu V (V - V_{cr})}{R^2 \ln(R/r)}. \quad (36)$$

In general cases, the corona discharge power can be determined based on equation (34) as

$$P = CV(V - V_{cr}). \quad (37)$$

For example, corona discharges generated in atmospheric pressure air around a thin wire ( $r = 0.1 \text{ cm}$ ,  $R = 10 \text{ cm}$ ,  $V_{cr} = 30 \text{ kV}$ ) with voltage 40 kV releases a power of about  $0.2 \text{ W cm}^{-1}$  of the discharge.

The power of the continuous corona discharges is very low and not acceptable for many applications, and a further

increase of voltage and current leads to corona transition into sparks. However, these can be prevented by organizing the corona discharge in a pulse-periodic mode. Such pulsed corona discharges will be discussed in the next section.

Although the corona power is relatively low per unit length of a wire, the total corona power becomes significant when the wires are very long. Such situations occur in the case of high voltage overland transmission lines, where coronal losses are significant. In humid and snowy conditions, these can exceed the resistive losses.

In the case of high voltage overland transmission lines, the two wires generate corona discharges of opposite polarity. Electric currents outside the active volumes of the opposite polarity corona discharges are provided by positive and negative ions moving in opposite directions. These positive and negative ions meet and neutralize each other between wires, which results in a decrease of the space charge and an increase of the corona current, which leads to phenomenal power losses.

## 4. The pulsed corona discharge

### 4.1. Overview of the pulsed corona discharge

Corona discharges are very attractive for different modern industrial applications, such as surface treatment and cleansing of gas and liquid exhaust streams. These discharges are able to generate a high concentration of active atoms and radicals at atmospheric pressure without heating the gas volume.

As was shown previously, the application of the continuous corona discharge is limited by very low currents and, hence, very low power of the discharge resulting in a low rate of treatment of materials and exhaust streams.

An increase in corona voltage and power without spark formation becomes possible by using pulse-periodic voltages. Currently, the pulsed corona is one of the most promising atmospheric pressure, non-thermal discharges. The streamer velocity is about  $10^8 \text{ cm s}^{-1}$  and exceeds by a factor of 10 the typical electron drift velocity in an avalanche. If the distance between electrodes is about 1–3 cm, the total time necessary for the development of avalanches, avalanche-to-streamer transition and streamer propagation between electrodes is about 100–300 ns. This means that voltage pulses of this duration are able to sustain streamers and effective power transfer into non-thermal plasma without streamer transformations into sparks.

For the pulsed corona discharges it is important to make pulsed power supplies, capable of generating sufficiently short voltage pulses with steep front and very short rise times. Some specific methods of generation and parameters for the pulsed corona discharges will be discussed later in this section. First, we discuss some important non-steady-state phenomena occurring in the continuous corona discharges, which should be taken into account in analysing pulsed corona discharges.

### 4.2. Corona ignition delay

Ignition of the negative corona involves the same mechanism as in Townsend breakdown. Thus, ignition delay of the continuous negative corona strongly depends on cathode conditions and varies from one experiment to another. Such

facility specific characteristics are one reason why pulsed coronas are more often organized as positive ones. The typical ignition delay in the case of positive coronas is about 100 ns and, in contrast with the negative corona, it is not sensitive to the cathode conditions, because the streamer breakdown mechanism is responsible for ignition. The ignition delay is much longer than streamer propagation times, because it is related to the time for initial electron formation and propagation of initial avalanches.

Random electrons in the atmosphere usually exist in the form of negative ions, their effective detachment is due to ion–neutral collisions and effectively takes place at electric fields of about  $70 \text{ kV cm}^{-1}$ . If humidity is high and the negative ions are hydrated, the electric field necessary for detachment and formation of a free electron is slightly higher.

Thus, experimental data related to the ignition delay of the continuous corona actually indicate the same limits for pulse duration in pulsed corona discharges. This means that there are some advantages for the positive corona and the cathode-directed streamers, and also shows the electric fields necessary for the effective release of initial free electrons by detachment from negative ions.

### 4.3. Flashing corona

Corona discharges sometimes operate in the form of periodic current pulses even under constant voltage conditions. The frequency of these pulses can reach  $10^3 \text{ Hz}$  in the case of positive coronas and  $10^6 \text{ Hz}$  for negative coronas. This self-organized pulsed corona discharge is obviously unable to overcome the current and power limitations of the continuous corona discharges, because continuous high voltage still promotes the corona-to-spark transition. However, it is an important step towards non-steady-state coronas with higher voltages, higher currents and higher power.

The flashing corona phenomenon can be explained by the effect of positive space charge, which is created when electrons formed in streamers decrease fast at the anode but slow positive ions remain in the discharge gap. The growing positive space charge causes a decrease in the electric field near the anode and prevents the generation of new streamers. Positive corona current is suppressed until the positive space charge goes to the cathode and clears the discharge gap. After that a new corona ignition takes place and the cycle can be repeated again.

The flashing corona phenomenon does not occur at intermediate voltages, when the electric field outside the active corona volume is sufficiently high to provide effective steady-state clearance of positive ions from the discharge gap, but not too high to provide intensive ionization. It is interesting to note that the electric current in the flashing corona regime does not fall to zero between pulses, some constant component of the corona current is continuously present.

The pulse-periodic regime leads to a fundamental increase of corona power. However, the power increase in this system is still limited by spark formation because the applied voltage is continuous.

### 4.4. Trichel pulses

Negative corona discharges sustained by continuous voltage can also operate in the pulse-periodic regime at relatively

low values of voltages close to the ignition value. The pulse duration in negative corona is short, approximately 100 ns. If the mean corona current is  $20 \mu\text{A}$ , the peak value of current in each pulse can reach 10 mA. The pulses disappear at higher voltages, and in contrast to the case of positive corona the steady-state discharge exists till transition to spark.

The pulse-periodic regime of the negative corona discharge is usually referred to as Trichel pulses. Trichel pulses are similar to those of the flashing corona discussed above, though with some peculiarities. The growth of avalanches from the cathode leads to the formation of two charged layers: (a) an internal one, which is positive and consists of positive ions; (b) an external one, which is negative and consists of either negative ions (in air or other electronegative gases) or electrons in the case of electropositive gases.

The Trichel pulses are not generated in electropositive gases. Because of the high mobility of the electrons, they reach an anode quite fast. As a result, the density of the space charge of electrons in the external layer is very low and, consequently, the electric field near the cathode is not suppressed. The positively charged internal layer even increases the electric field in the vicinity of the cathode, and provides even better conditions for the active corona volume. Thus, only electronegative gases may sustain the Trichel pulses.

The negative ions in electronegative gases form a significant negative space charge around the cathode, which cannot be compensated by the narrow layer of positive ions. Thus, the space charge of the negative ions suppresses the electric field near the cathode and, hence, suppresses the corona current. Subsequently, when the ions leave the discharge gap and are neutralized on the electrodes, the negative corona can be re-ignited, and the cycle can be repeated again.

#### 4.5. Pulsed corona discharges sustained by nano-second pulsed power supplies

Pulsed corona discharges sustained by nano-second pulsed power supplies generate pulses with durations in the range 100–300 ns and sufficiently short to avoid the corona-to-spark transition. The power supply should provide a pretty high voltage rise rate ( $0.5\text{--}3 \text{ kV ns}^{-1}$ ), which results in higher corona ignition voltage and higher power. As an illustration of this effect, figure 5 shows the corona inception voltage as a function of the voltage rise rate [14].

The high voltage rise rates also results in better efficiency of several plasma-chemical processes requiring higher electron energies. In these plasma-chemical processes (i.e. plasma cleansing of gas and liquid streams) high values of mean electron energy are necessary to decrease the fraction of the discharge power going to vibrational excitation of molecules, and stimulate ionization and electronic excitation and dissociation of molecules.

The nano-second pulsed power supply technology is used in different applications such as Marx generators, simple and rotating spark gaps, electronic lamps, thyatrons and thyristors with possible further magnetic compression of pulses (see, e.g., [15]) and transistors for high voltage pulse generation.

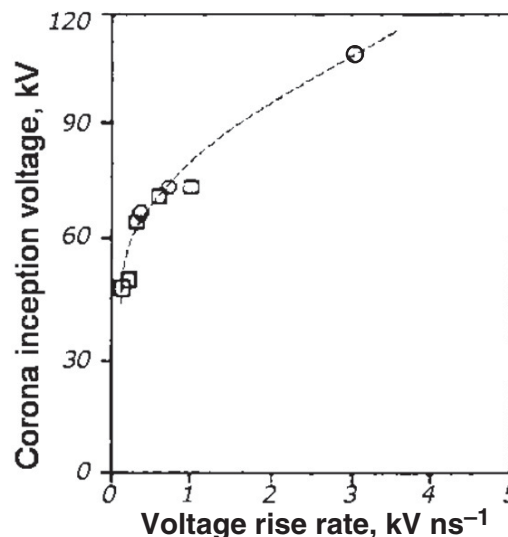


Figure 5. Corona inception voltage as a function of the voltage rise rate.

In general, the pulsed corona can be relatively powerful, luminous and quite nice looking. More information about the physical aspects and applications of the pulsed corona discharge can be found in [16–18]. An example of a practical application of the pulsed corona discharge is a pilot plant for treatment of VOC emissions in the paper industry developed in Drexel Plasma Institute; see figure 6.

#### 4.6. Configurations of the pulsed corona discharges

The most typical configurations of the pulsed corona as well as continuous corona discharges involve the use of thin wires, which maximize the active discharge volume. One of these configurations is illustrated in figure 7. Limitations of the wire configuration of the corona are related to the durability of the electrodes and also to the non-optimal interaction of the discharge volume with the incoming gas flow, which is important for plasma-chemical applications.

From this point of view, it is useful to use another corona discharge configuration, based on multiple stages of pin-to-plate electrodes [19]. This system is obviously more durable and it is able to provide good interaction of the incoming gas stream with the active corona volume formed in between the electrodes with pins and holes.

Combination of pulsed corona discharges with other methods of gas treatment is very practical for different applications. For example, the pulsed corona was successfully combined with catalysis to achieve improved results in the plasma treatment of automotive exhausts [17], and for hydrogen production from heavy hydrocarbons [20].

Another interesting technological hybrid is related to the pulsed corona coupled with water flow. Such a system can be arranged either in the form of a shower, which is called the spray corona, or as a thin water film on the walls, which is usually referred to as the wet corona (see figure 8). Such plasma scrubbers are especially effective in air cleansing processes, when the plasma just converts a non-soluble pollutant into a soluble one.

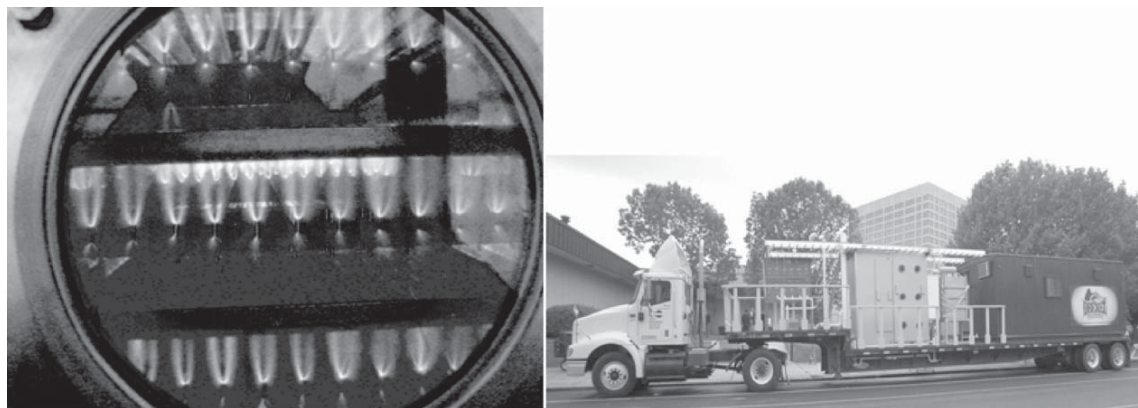


**Figure 6.** Large-volume, atmospheric pressure pulsed discharge plasma for treating VOC emissions. Left picture: discharge operation at 4 kW. Right picture: overview of the discharge system—pilot plant.

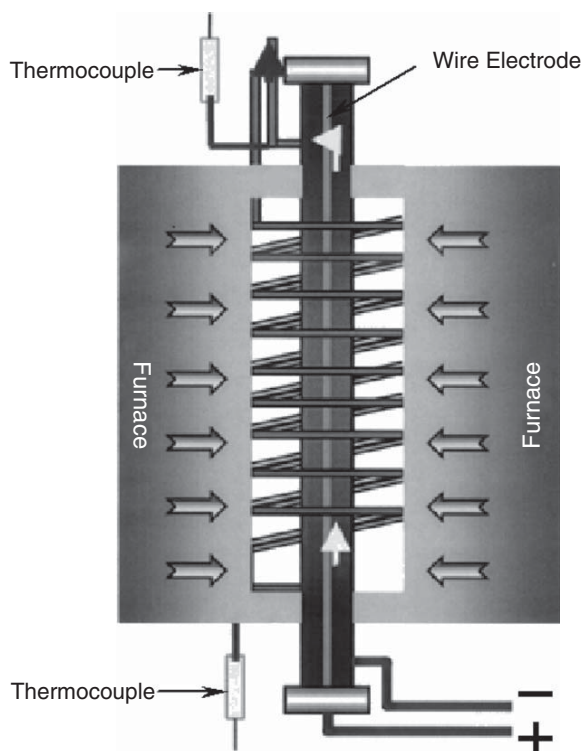


**Figure 7.** Pulsed corona discharge in wire cylinder configuration with preheating.

## 5. Dielectric-barrier discharge

### 5.1. Overview of the DBD

As was discussed before, the corona-to-spark transition can be prevented in pulsed corona discharges by employing nano-second pulsed power supplies. There is also another approach that helps in avoiding spark formation in streamer channels. This approach is based on the use of a dielectric barrier in the discharge gap, which stops electric current and prevents spark formation. Such a discharge system is called a DBD. The presence of a dielectric barrier precludes dc operation of

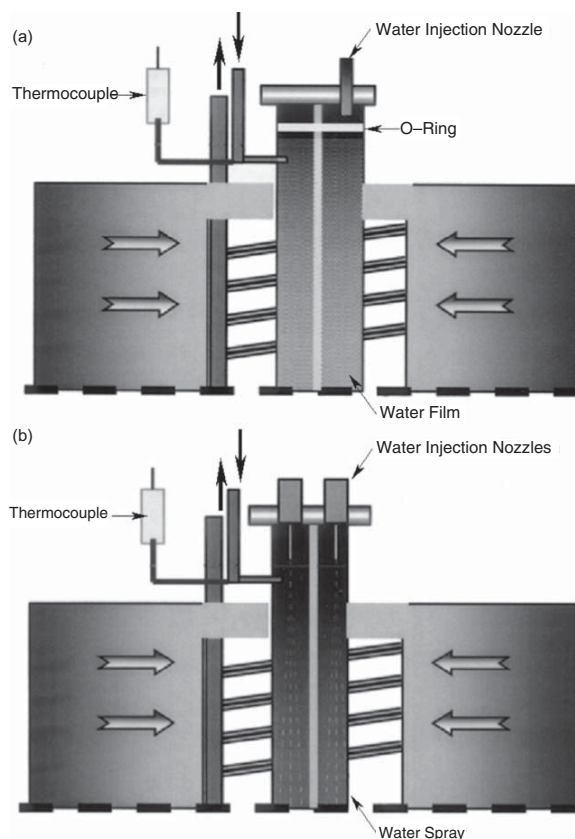


**Figure 8.** Modification of corona discharge shown in figure 7: wet (a) and spray (b) corona discharges.

DBD, which usually operates at frequencies between 0.05 and 500 kHz. Sometimes DBDs are also called silent discharges, due to the absence of sparks, which are accompanied by local overheating, generation of local shock waves and noise.

DBDs have a large number of industrial applications because they operate at strongly non-equilibrium conditions at atmospheric pressure and at reasonably high power levels, without using sophisticated pulsed power supplies.

This discharge is industrially applied in ozone generation, CO<sub>2</sub> lasers, and as a UV-source in excimer lamps. In addition, the DBD in air is commonly used in the web conversion industry where it is known commercially as ‘corona discharge treatment’. It is used to treat polymer surfaces in order to promote wettability, printability and adhesion [70]. This non-equilibrium discharge is especially advantageous for the web conversion industry because it operates at atmospheric pressure and ambient temperature. The use of the so-called ‘corona treatment’, as well as other various surface modification methods for the manufacture of many different types of products on moving webs, is extensively described in the literature [71]. DBD application for pollution control is quite promising, but the largest expected DBD application is related to plasma display panels for large-area flat television screens. Strong thermodynamic non-equilibrium and simple design are the distinctive properties of DBD that allow us to envisage expansion of its applications in low temperature atmospheric pressure plasma chemistry. DBDs have much potential in the prospective technology of exhaust cleaning from CO, NO<sub>x</sub> and VOCs [72]. Successful use of DBDs reported in recent research on plasma-assisted combustion may result in new applications [73].

Important contributions to the fundamental understanding and industrial applications of DBD were made recently by Kogelschatz *et al* [21] at ABB. However, this discharge actually has a long history. It was first introduced by Siemens [22] in 1857 to create ozone, which determined the main direction for investigations and applications of this discharge for many decades. Important steps in understanding the physical nature of the DBD were made by Klemenc in 1937 [23]. Their work showed that this discharge occurs in a number of individual tiny breakdown channels, which are now referred to as microdischarges; these authors intensively investigated their relationship with streamers.

## 5.2. Properties of the DBDs

The DBD gap usually includes one or more dielectric layers, which are located in the current path between metal electrodes. Two specific DBD configurations, planar and cylindrical, are illustrated in figure 9 [24]. The typical clearance in the discharge gaps varies from 0.1 mm to several centimetres.

The breakdown voltages of these gaps with dielectric barriers are practically the same as those between metal electrodes. If the DBD gap is a few millimetres, the required AC driving voltage with frequency 500 Hz to 500 kHz is typically about 10 kV at atmospheric pressure.

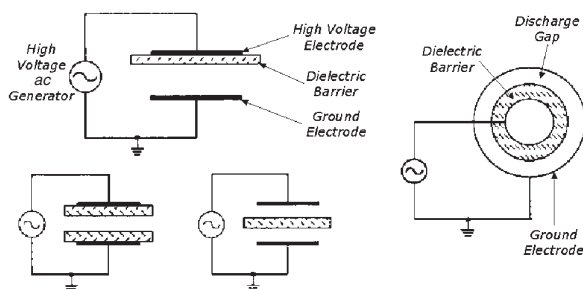


Figure 9. Common DBD configurations [24].

The dielectric barrier can be made from glass, quartz, ceramics or other materials of low dielectric loss and high breakdown strength. Then, a metal electrode coating can be applied to the dielectric barrier. The barrier–electrode combination also can be arranged in the opposite manner, e.g. metal electrodes can be coated by a dielectric. As an example, steel tubes coated by an enamel layer can be effectively used in the DBD.

In most cases, DBDs are not uniform and consist of numerous microdischarges distributed in the discharge gap, as can be seen from figure 10. The physics of microdischarges is based on an understanding of the formation and propagation of streamers, and consequent plasma channel degradation. The electrons in the conducting plasma channel established by the streamers dissipate from the gap in about 40 ns, while the heavy and slowly drifting ions remain in the discharge gap for several microseconds (table 3). Deposition of electrons from the conducting channel onto the anode dielectric barrier results in charge accumulation and prevents new avalanches and streamers nearby until the cathode and anode are reversed (if the applied voltage is not much higher than the voltage necessary for breakdown). The usual operation frequency used in the DBDs is around 20 kHz; therefore, the voltage polarity reversal occurs within 25  $\mu$ s. After the voltage polarity reverses, the deposited negative charge facilitates the formation of new avalanches and streamers in the same spot. As a result,

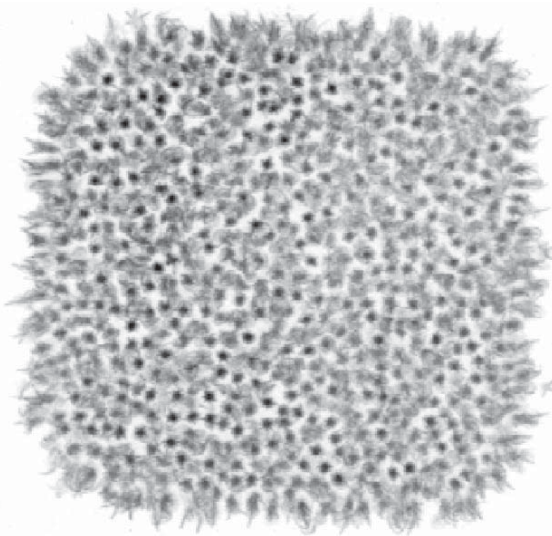


Figure 10. The storage phosphor image of filaments in the DBD gap in air obtained from an experimental set-up using ten excitation cycles at 20.9 kHz and a discharge gap of 0.762 mm; the discharge area is 5 cm  $\times$  5 cm.

Table 3. Calculated microdischarge characteristics for DBDs (1 mm gap, air, 1 atm).

	Duration	Charge transferred
Microdischarge (0.2 mm radius)	40 ns	$10^{-9}$ C
• Electron avalanche	10 ns	$10^{-11}$ C
• Cathode-directed streamer	1 ns	$10^{-10}$ C
• Plasma channel	30 ns	$10^{-9}$ C
Microdischarge remnant	1 ms	$\geq 10^{-9}$ C

a many-generation family of streamers is formed, which is macroscopically observed as a bright filament that appears to be spatially localized. It is important to clarify and distinguish the terms streamer and microdischarge. An initial electron starting from some point in the discharge gap (or from the cathode or dielectric that covers the cathode in the case of well-developed DBDs) produces secondary electrons by direct ionization and develops an electron *avalanche*. If the avalanche is large enough (Meek condition), a cathode-directed streamer is initiated (usually from the anode region). The streamer bridges the gap in a few nanoseconds and forms a conducting *channel* of weakly ionized plasma. Intense electron current will flow through this plasma channel until the local electric field collapses. Collapse of the local electric field is caused by the charges accumulated on the dielectric surface and ionic space charge (ions are too slow to leave the gap for the duration of this current peak). The group of local processes in the discharge gap initiated by the avalanche and developed until electron current termination is usually called a *microdischarge*. After electron current termination there is no more electron-ion plasma in the main part of the microdischarge channel, but the high level of vibrational and electronic excitation in the channel volume along with charges deposited on the surface and ionic charges in the volume allow us to separate this region from the rest of the volume, and we call it the microdischarge *remnant*. Positive ions (or positive and negative ions in the case of an electronegative gas) of the remnant slowly move to the electrodes resulting in low and very long ( $\sim 10 \mu\text{s}$  for 1 mm gap) falling ion current. The microdischarge remnant will facilitate the formation of new microdischarges in the same spot as the polarity of the applied voltage changes. That is why it is possible to see single *filaments* in DBD. If microdischarges formed at a new spot each time the polarity changed, the discharge would appear uniform. Thus, a *filament* in DBD is a group of microdischarges that form on the same spot each time the polarity is changed. The fact that the microdischarge remnant is not fully dissipated before the formation of the next microdischarge is called the memory effect.

Typical characteristics of DBD microdischarges in a 1 mm gap in atmospheric air are summarized in table 4.

A snapshot of the microdischarges in a 0.762 mm DBD air gap photographed through a transparent electrode is shown in figure 10. It can be seen that the microdischarges are spread over the whole DBD zone, quite uniformly.

Charge accumulation on the surface of the dielectric barrier reduces the electric field at the location of a microdischarge. These result in current termination within just several nanoseconds after breakdown (see table 3). The short duration of microdischarges leads to very low overheating of the streamer channel, and the DBD plasma remains strongly non-thermal.

The principal microdischarge properties for most of the frequencies do not depend on the characteristics of the external circuit, but only on the gas composition, pressure and the electrode configuration. An increase of power just leads to the generation of a larger number of microdischarges per unit time, which simplifies scaling of the DBDs.

Modelling of the microdischarges is closely related to the analysis of the avalanche-to-streamer transition and streamer propagation. Detailed two-dimensional modelling of the formation and propagation of relevant streamers can be found in numerous publications [25–29].

Interesting phenomena can occur due to the mutual influence of microdischarges in a DBD. These are related to the electrical interaction of microdischarges with residual charge left on the dielectric barrier and with the influence of excited species generated in one microdischarge on the formation of another microdischarge [30].

### 5.3. Phenomena of microdischarge interaction: pattern formation

Although DBDs have been intensively studied for the past century, the microdischarge interaction was discovered only recently [31]. This interaction is responsible for the formation of microdischarge patterns reminiscent of two-dimensional crystals (figure 10). Depending on the application, microdischarge patterns may have a significant influence on DBD performance, particularly when spatial uniformity is required.

The formation of microdischarges in DBDs was discussed in the previous section. The charge distribution associated with streamers and the local electric field in the gap associated with the plasma channel and microdischarge remnant is illustrated in figure 11. The left-hand side of figure 11 shows a streamer propagating from the anode to the cathode while attracting additional avalanches. The resulting plasma channel and microdischarge remnant that forms, shown on the right-hand side of the figure, have a net positive charge because the electrons leave the gap much faster than ions. The residual positive charge (together with the deposited negative charge in the case of the dielectric surface) influences the formation of nearby families of avalanches and streamers and, therefore, the formation of neighbouring microdischarges. The mechanism of influence is the following: positive charge (or dipole field in the case of deposited negative charge) intensifies the electric field in the cathode area of the neighbouring microdischarge and decreases the electric field in the anode area. Since the avalanche-to-streamer transition depends mostly on the near-anode electric field (from which new streamers originate), the formation of neighbouring microdischarges is actually prevented, and microdischarges effectively repel each other. This quasi-repulsion between microdischarges leads to the formation of short-range order that is related to a characteristic

**Table 4.** Typical parameters of a microdischarge.

Lifetime	1–20 ns	Filament radius	50–100 $\mu\text{m}$
Peak current	0.1 A	Current density	0.1–1 $\text{kA cm}^{-2}$
Electron density	$10^{14}$ – $10^{15} \text{ cm}^{-3}$	Electron energy	1–10 eV
Total transported charge	0.1–1 nC	Reduced electric field	$E/n = (1-2)(E/n)_{\text{Paschen}}$
Total dissipated energy	5 $\mu\text{J}$	Gas temperature	Close to average, about 300 K
Overheating	5 K		

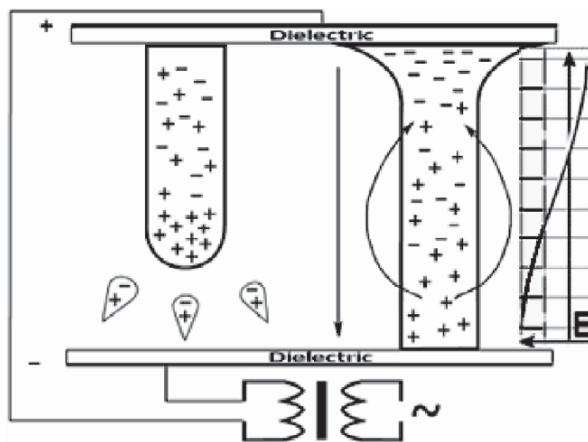


**Figure 11.** Illustration of electric field distortion caused by microdischarge remnants. Streamer formation (left side) and plasma channel (and microdischarge remnant) electric field distortion (right side) are due to space charges. The solid curve is the superposition of the electric field from the microdischarge and the applied electric field; the dashed line is the applied electric field. In the presence of a space positive charge, the electric field is increased at the cathode and decreased at the anode.

repulsion distance between microdischarges. Observation of this cooperative phenomenon depends on several factors, including the number of microdischarges occurring and the operating frequency. For example, when the number of microdischarges is not large enough (when the average distance between microdischarges is larger than the characteristic interaction radius), no significant microdischarge interaction is observed. When the AC frequency is too low to keep the microdischarge remnants from dissipation (low frequency means that the period is longer than the typical life time of the microdischarge remnant or ‘memory effect’ life time), microdischarge repulsion effects are not observed.

In addition, DBD cells operated at very high frequencies in the megahertz region will not exhibit microdischarge repulsion because the very high frequency switching of the voltage interferes with ions still moving to electrodes (for a detailed explanation of the ion trapping effect and an estimation of the frequency at which it becomes significant see [30]). The formation of microdischarge patterns in DBDs has been investigated both from theoretical and experimental perspectives [31].

The experimental image shown in figure 10 suggests that filaments (microdischarge families) space themselves out. To model the interaction between microdischarges, it can be assumed that avalanche to streamer transition depends only on the local value of the electric field and the discharge gap. Once the microdischarge is formed, the electric field of the microdischarge remnant decreases the external applied electric field in the fashion described above. The average effective field in the local region near the anode where the avalanche to streamer transition occurs decreases and, as a consequence, the formation of new streamers at the same location is prevented unless there is an increase in the external applied voltage. We should emphasize that observation of microdischarge filaments in DBDs is possible when both electrodes are covered by a dielectric as well as in the case when one electrode is not

covered, meaning that no surface discharge can be deposited on this electrode. Thus, repetition of microdischarges at the same spot depends on the volume charge mostly, and surface charge deposition is not critical. When the externally applied field varies quickly with respect to the microdischarge remnant dissipation lifetime in the system, the microdischarges will stay separated by a distance corresponding to the length scale of the field inhomogeneity. If the applied electric field is high enough, it will cause microdischarges to develop in all the unoccupied spaces, so that the gap becomes filled from end to end.

In the unipolar or dc case (before the polarity changes), one of the electrodes remains positive and the other is negative. The streamer always moves in one direction so that subsequent streamers and thus microdischarges have a small probability of forming in the same place until the microdischarge remnant has dispersed. A different situation arises in the case of alternating voltage. There is no need to wait until the microdischarge remnant dissipates. Instead, the probability of appearance of a streamer in the location of the microdischarge remnant increases when the voltage is switched. After the voltage is switched, the electric field of the microdischarge remnant adds to the strength of the applied electric field thereby increasing the local field. The increased electric field increases the likelihood for a new streamer to occur at the same place. The net result is that if the original streamer formed just before voltage switching, there is an increased probability of streamers occurring in the same place or nearest vicinity. The remainder of this section describes the Monte Carlo approach that is useful for the simulation of microdischarge interactions.

The general cellular automata (CA) scheme consists of a lattice of cells that can have any dimension and size, coupled with a set of rules for determining the state of the cells. At any time a cell can be in only one state. From a physical perspective, each cell represents a volume in the gap located between the electrode surfaces. The upper and lower surfaces of each cell are bounded by the dielectric surfaces of the electrodes themselves, and the height of each cell is defined by the gap distance. The CA transformation rules define a new state for a cell after a given time step, using data about the states of all the cells in the CA and additional information, such as the driving voltages imposed upon the system as a whole. It is assumed that the probability for the occurrence of the streamer depends only on the local value of the electric field. The position of a streamer strike is determined using a Monte Carlo decision for given probability values in each cell. Once the position of the streamer strike is known, the plasma channel is formed at the same place and the total charge transferred by this microdischarge is assigned to the cell to be used later in electric field calculations. Since the time lag between streamers is random, an additional Monte Carlo simulation was used to decide whether a streamer will occur or not. If the streamer does not strike the plasma channel will not be formed and there will be no microdischarge.

It is not necessary to specify the charge transferred by the microdischarge, instead, it can be dynamically calculated during simulation based on the local electric field strength. The charge transferred by an individual microdischarge decreases the electric field inside the microdischarge channel because it creates a local electric field opposing the externally

applied electric field (the collapse of the electric field in the microdischarge channel). Thus, the total charge transferred by the microdischarge is the amount of charge that decreases the local electric field to zero (in other words, the charge passes through the microdischarge channel established in a CA cell until the local electric field drops to zero). Although it seems not to be the case, especially in electronegative gases (the electric field does not collapse to zero), this assumption is good enough to represent interaction between microdischarges.

The probability of a streamer striking is calculated from the local electric field using the following formula:

$$P(E) = 1 - \frac{1}{1 + \exp(S((E - E_0)/E_0))}, \quad (38)$$

where  $E$  is the electric field in the cell,  $E_0$  the critical electric field necessary for streamer formation given by the Meek condition and  $S$  is a parameter related to the ability of the discharge to accumulate memory about previous microdischarges. When  $S$  is large, the memory effect has a negligible influence on the operation of DBDs, and the probability function will be a step function that represents the Meek condition for streamer formation. When  $S$  is small, the memory effect significantly affects the probability of streamer formation. It is known that streamer formation is influenced by a number of factors. The presence of the vibrationally and electronically excited species and negative ions increases the ionization coefficient (first Townsend coefficient) and thus lowers the electric field required for avalanche to streamer transition. Furthermore, the discharge operating frequency also influences streamer formation so the memory effect is frequency dependent. In light of all the factors that influence streamer formation, the value of  $S$  is best determined empirically from experimental data.

The typical results of simulation can be seen in figure 12. The grey scale intensity at any particular cell is proportional



**Figure 12.** The enlarged central portion of a simulated microdischarge pattern in DBD. Simulation conditions are the same as for the experimental image in figure 10. The size of the microdischarge footprint is the same as in figure 10.

to the number of streamers striking the cell. The simulation shows that the occurrence of microdischarges across the simulation lattice is non-uniform: some regions are well treated by microdischarges and some are not treated at all. This non-uniformity is the result of interactions between microdischarges. Simulation results for image analysis were post-processed for better comparison with experimental images. The intensity of a microdischarge feature in a cell is given by the simulation, and the location of the microdischarge is assumed to be at the centre point of the cell. The size of each circular microdischarge feature is taken as the theoretically calculated diameter of the plasma channel. This information was used to construct a digital image with a pixel size equivalent to that in the experimental images.

Experimental results as well as theoretical ones derived from our probabilistic models are images with features that correspond to microdischarges. It is natural, then, to consider image analysis methods as a technique to make comparisons. Although there are many possible methods that could be employed for this purpose, the two-dimensional correlation function and the Voronoi polyhedron approach proved to be the most useful.

Voronoi polyhedra analysis defines polyhedral cells around selected features in an image, and the distribution of polyhedra types in the analysis can be used as a comparative tool. Voronoi polyhedra analysis is an excellent tool for measuring homogeneity of patterns as well as for comparison of different patterns. Homogeneity can be easily estimated from distributions of the Voronoi cell surface areas and used for comparison. Also, the topology of the pattern can be compared using the distribution of the number of sides of Voronoi cells. This type of comparison is extremely useful in our case as it is invariant to stretching and rotation of the patterns, and also invariant to the particular positions of the microdischarge footprints. Although microdischarge patterns were never analysed before using Voronoi polyhedra this type of analysis is a standard for analysis of Coulomb crystals. The Voronoi polyhedra analysis of an experimental image and its simulation is shown in figures 13 and 14, respectively. The Voronoi analysis of a random dot pattern is shown in figure 15 (case without microdischarge interaction). A comparison of the Voronoi analysis of the random dot pattern with the simulated and experimental results shows that the random pattern is very different. This demonstrates the importance of short-range interaction between microdischarges in DBD. One way to express numerically the difference between the images is to count the number of different-sided polyhedra determined in the Voronoi analysis. Unlike the random dot pattern, most of the polyhedral cells found in the analysis of the experimental and simulated images have six interior sides (six angles). This corresponds to the hexagonal lattice and thus implies radial symmetry of the interaction. This type of interaction was observed experimentally and was also predicted by the model.

The correlation function is widely used for post-processing in crystallography and can provide some indication of the correlation between features in a data set. The correlation function of the experimental image and the simulation is shown in figure 16 with open and solid symbols, respectively. The correlation function for random dots is shown in figure 16 as a plain line. As is expected,

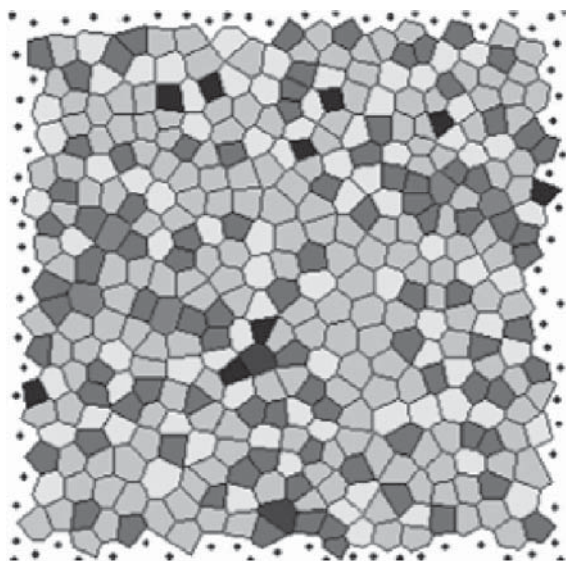


**Figure 13.** Voronoi polyhedra analysis of the experimentally obtained microdischarge locations from the image shown in figure 10. The polyhedra cells are colour coded according to the number of angles in each polyhedron. The cells in the image, obtained experimentally, are mainly six-sided cells and have similar sizes.

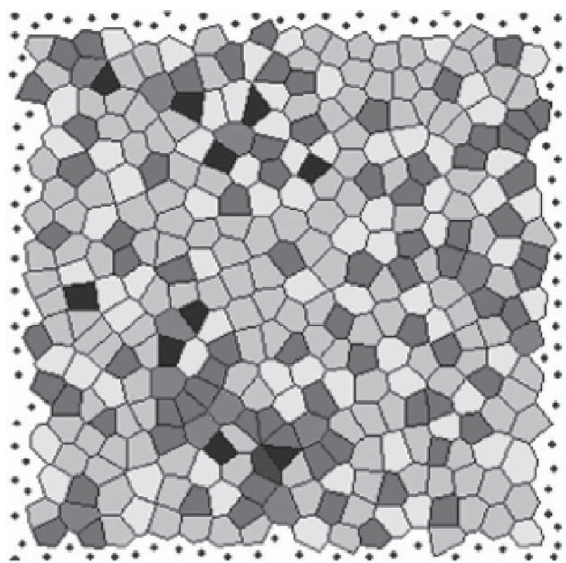


**Figure 14.** Voronoi polyhedra analysis of the simulated microdischarge locations from the image shown in figure 12. The polyhedra cells are colour coded according to the number of angles in each polyhedron. The cells in the image obtained in simulation are mainly six-sided cells and have similar sizes.

a random distribution of dots on a plane does not show any periodic oscillations in the correlation function. The correlation function for a completely ordered lattice should show strong oscillations or peaks indicating that all the features in the image are related by well-defined unit cell vectors. As spatial correlation between features in the image decreases, the peaks in the correlation function level off. For example, the correlation function for a two-dimensional

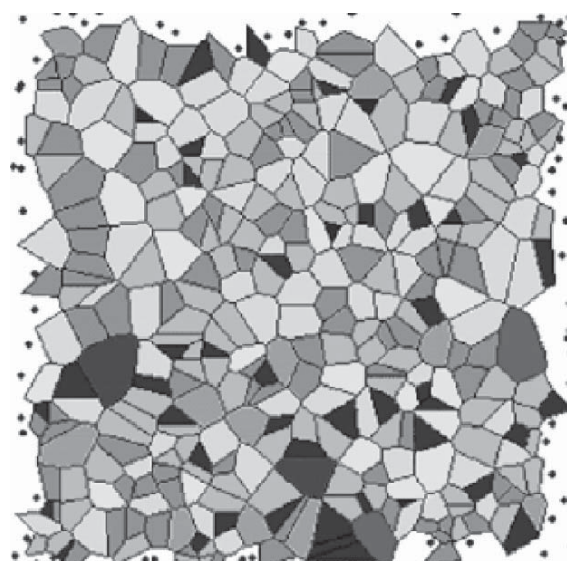


**Figure 15.** Voronoi polyhedra analysis of a random dot pattern for comparison with figures 13 and 14. The polyhedra cells are colour coded according to the number of angles in each polyhedron. The areas of different cells vary significantly.

liquid with short-range correlation will look similar to experimental and modelling curves in figure 16, where the strong oscillation shows up at short distances and then dampens out as a result of disorder. The overall agreement of the correlation function plots for the experimental and simulated images demonstrates that the features observed in the experimental image are not arranged randomly but are strongly influenced by microdischarge interactions in the DBD. It was found that under certain conditions streamers in DBDs do not strike randomly and the microdischarges they form interact and arrange themselves into a regular filament pattern. The obtained discharge images suggest that short-range interactions between microdischarges are present in the discharge.

The microdischarge interaction model based on the assumption that avalanche to streamer transition and microdischarge formation are influenced by the microdischarge remnants, allows us to simulate microdischarge interaction and pattern formation. Simulation results show qualitative agreement with experimental ones and demonstrate the importance of microdischarge interaction in barrier discharges. A short-range interaction between microdischarges and the resulting filament pattern can be predicted using a model of interaction.

Using Voronoi polyhedra analysis, simulation results were compared with experimental ones yielding convincing evidence of microdischarge interactions in DBDs, and demonstrating the validity of the model and assumptions.

#### 5.4. Surface discharges

Closely related to the DBD are surface discharges, generated at dielectric surfaces embedded with metal electrodes in a different way. The dielectric surface essentially decreases the breakdown voltage in such systems, because of the creation of significant non-uniformities of the electric field and hence

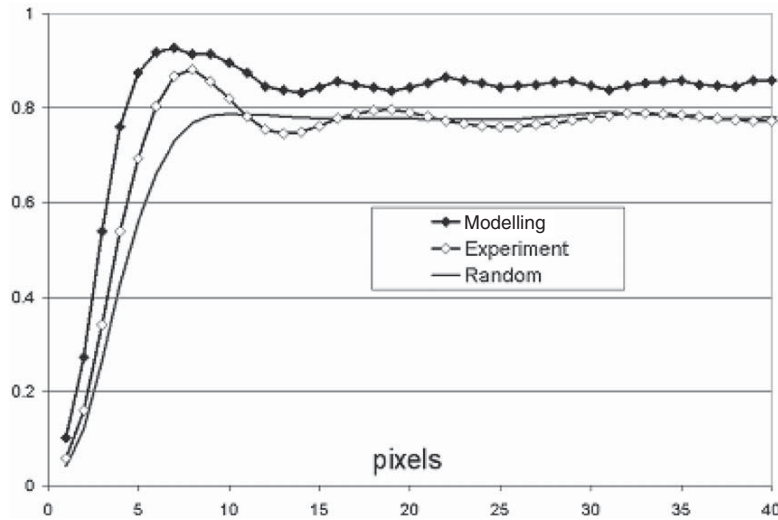


**Figure 16.** Two-dimensional correlation functions of: (open signs) experimental image from figure 13; (solid signs) simulation data from figure 14; and (no signs) data from random-point distribution (shown for comparison).

creates a local overvoltage. The surface discharges, as well as DBDs, can be supplied by AC or pulsed voltage.

A very effective decrease of the breakdown voltage can be reached in the surface discharge configuration, where one electrode just lies on the dielectric plate, with another one partially wrapped around [32]. This discharge is called a sliding discharge. It can be pretty uniform in some regimes on the dielectric plates of high surface area with linear sizes over 1 m at voltages not exceeding 20 kV.

The component of electric field  $E_y$  normal to the dielectric surface plays an important role in the generation of the pulsed-periodic sliding discharge, which does not depend essentially on the distance between electrodes along the dielectric. That is why breakdown voltages of the sliding discharge do not follow the Paschen law.

Two qualitatively different modes of the surface discharges can be achieved by changing the applied voltage amplitude: a complete one (sliding surface spark) and an incomplete one (sliding surface corona). Pictures of these discharges are presented in figure 17. The sliding surface corona discharge ignites at voltages below the critical breakdown value and has a low current limited by charging the dielectric capacitance. The active volume and luminosity of this discharge are localized near the igniting electrode and do not cover the whole dielectric.

The sliding surface spark (or the complete surface discharge) takes place at voltages exceeding the critical one corresponding to breakdown. Here, the plasma channels formed actually connect electrodes of the surface discharge gap. At low overvoltages, the breakdown delay is about  $1 \mu\text{s}$ . In this case, the many step breakdown phenomenon starts with the propagation of a direct ionization wave, which is followed by a possible more intense reverse wave related to the compensation of charges left on the dielectric surface. After about  $0.1 \mu\text{s}$ , the complete surface discharge covers the entire electrode of the discharge gap. The sliding spark at low overvoltage usually consists of only one or two current channels.

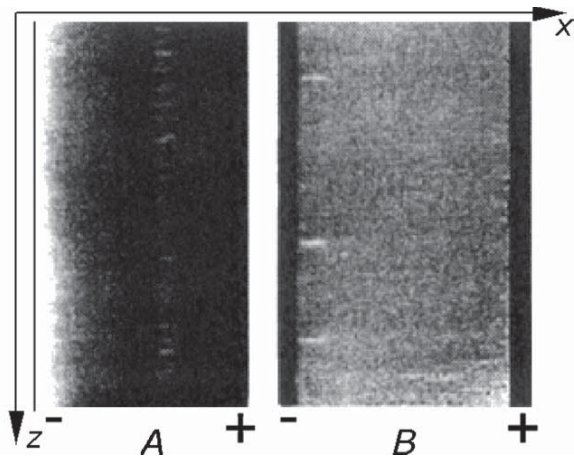


**Figure 17.** Complete (B) and incomplete (A) surface discharges (He,  $p = 1 \text{ atm}$ ,  $\varepsilon \approx 5$ ,  $d = 0.5 \text{ mm}$ , pulse frequency  $6 \times 10^{13} \text{ Hz}$ ) in parallel plate electrode configuration. The cathode is on the left in both pictures [76].

At higher overvoltages, the breakdown delay becomes shorter, reaching the nanosecond time scale. In this case, the complete discharge regime takes place immediately after the direct ionization wave reaches the opposite electrode. The surface discharge consists of many current channels in this regime. In general, the sliding spark surface discharge is able to generate luminous current channels of very sophisticated shapes, usually referred to as Lichtenberg figures.

The number of channels  $r$  depends on the capacitance factor  $\varepsilon/d$  (ratio of the dielectric permittivity to the thickness of the dielectric layer), which determines the level of electric field on the sliding spark discharge surface. This effect is illustrated in figure 18 and is important in the formation of large area surface discharges with homogeneous luminosity. Many interesting additional details related to physical principles and applications of the sliding surface discharges can be found in [32].

### 5.5. The packed-bed corona discharge

The packed-bed corona is an interesting combination of the DBD and the sliding surface discharge. In this system, a high AC voltage (about 15–30 kV) is applied to a packed bed of dielectric pellets and creates a non-equilibrium plasma in the void between the pellets [33, 34]. The pellets effectively refract the high voltage electric field, making it essentially non-uniform and stronger than the externally applied field by a factor of 10–250, depending on the shape, porosity and dielectric constant of the pellet material.

A typical scheme for organizing a packed-bed corona is shown in figure 19(a); a picture of the discharge is presented in figure 19(b). The discharge chamber, shown in the figure, consists of coaxial cylinders with an inner metal electrode and

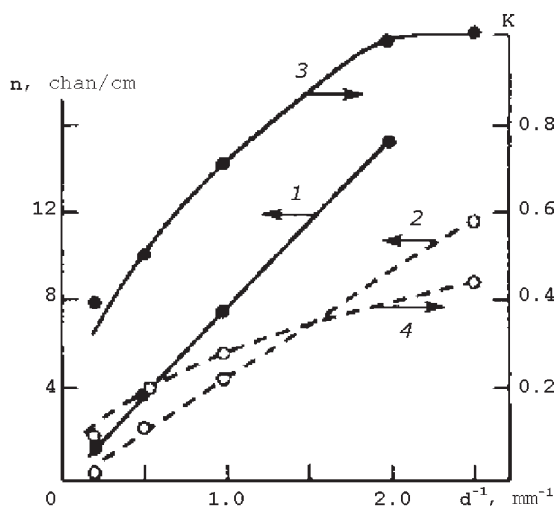


**Figure 18.** Linear density of channels  $n$  (1, 2) and surface coverage by plasma  $K$  (3, 4) as a function of  $d^{-1}$ , inverse dielectric thickness: He (1, 3), air (2, 4) [65].

an outer tube made of glass. The dielectric pellets are placed in the annular gap. A metal foil or screen in contact with the outside surface of the tube serves as the ground electrode. The inner electrode is connected to a high voltage AC power supply operated at the level of 15–30 kV, either at a fixed frequency of 60 Hz or at variable frequencies.

In this discharge system the glass tube serves as a dielectric barrier to inhibit direct charge transfer between electrodes and as a plasma-chemical reaction vessel. The packed-bed corona is specifically known for its applications in air purification systems and other environmental control processes.

### 5.6. Atmospheric pressure glow discharge

DBDs can exhibit two major discharge modes: filamentary mode and homogeneous or glow mode. The filamentary mode (that was discussed previously) has been a topic for active investigations in the past several years. A lot of experimental and theoretical work has been done in this area. Most industrial DBD applications utilize the filamentary mode. However, for a homogeneous treatment of surfaces, or for the deposition of thin films, the glow discharge mode has obvious advantages over the filamentary one. DBD glow mode or atmospheric pressure glow (APG) discharges with average power densities comparable to those of filamentary discharges will be of enormous interest for applications if reliable control over it could be achieved. Such discharges can be effectively organized in a DBD configuration. The APG discharge permits us to arrange the barrier discharge homogeneously without streamers and other spark-related phenomena. Practically, it is important that the glow mode of DBD can be operated at much lower voltages (down to hundreds volts) with respect to those of traditional DBD conditions.

A detailed explanation of the operation of APG discharges is not known. It is clear, however, that streamers can be avoided by using an applied electric field below the Meek criterion.

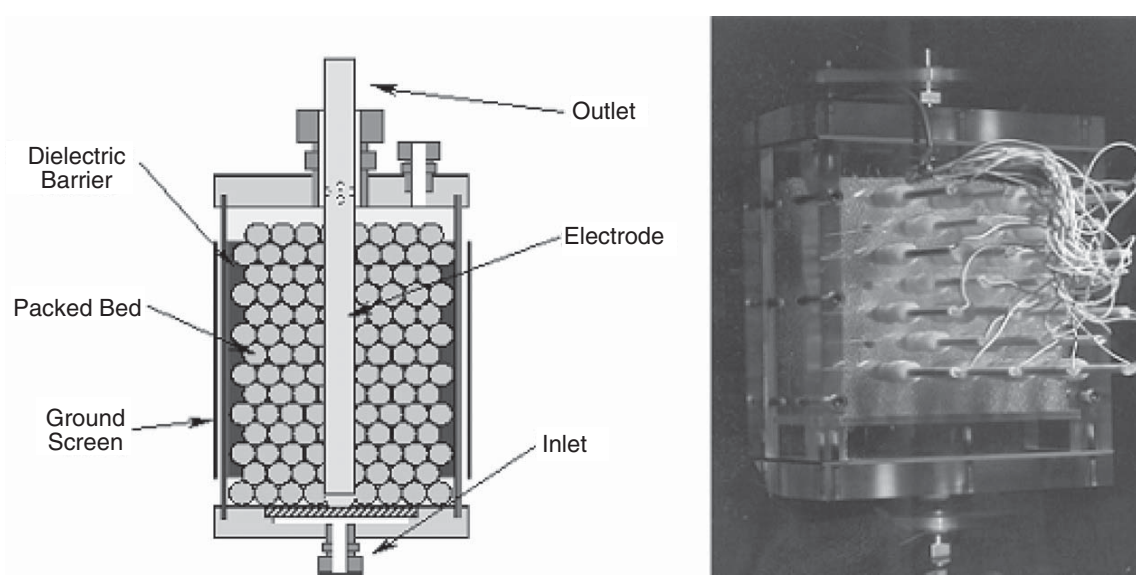


**Figure 19.** Packed-bed corona: scheme (a) and picture (b) [33].

If the electric field is less than that required by the Meek criterion for streamer formation, the discharge will operate in the avalanche mode because there will be no streamers. A discharge that operates in the avalanche mode and relies on occasional formation of primary electrons is usually called a dark discharge. Dark discharge current is limited by the rate of formation of occasional primary electrons, which is usually very low in the absence of an external ionization source. Because they are not self-sustained, dark discharges are very weak and thus useless for practical applications that require high specific power. One avalanche produces  $N_p = \exp(\alpha d) - 1$  positive ions. If these positive ions are able to cause the emission of at least one electron on average from the dielectric surface, a new avalanche will be formed and dark discharge will undergo the transition to a self-sustained Townsend discharge. Thus, the criterion for transition from dark to Townsend discharge is  $(\exp(\alpha d) - 1)\gamma > 1$ , where  $\gamma$  is the coefficient of secondary electron emission (also known as the third Townsend coefficient). The current of Townsend discharge is only limited by the external circuit and by charge accumulation on the dielectric surface. When the space charge in a Townsend discharge becomes large enough (when the discharge current increases above a certain value) to cause a significant disturbance of the applied electric field, the transition to glow discharge occurs [1].

Secondary emission from dielectric surfaces relies upon adsorbed electrons (with binding energy of about 1 eV) that were deposited during the previous excitation (high voltage) cycle. If enough electrons ‘survive’ the voltage switching time without recombining with positive ions (or attaching to form negative ions) they can trigger a transition from dark to Townsend mode of the discharge. The electron ‘survival’ time or memory effect is critical for the organization of APGs and depends on the properties of the dielectric surface as well as the operating gas [75]. It is clear that in electronegative gases the memory effect is weaker than in non-electronegative ones because of the loss of electrons due to attachment. If the memory effect is strong enough the transition from dark to Townsend mode can be accomplished, and a powerful uniform discharge can be obtained in the absence of streamers. A streamer discharge can always be produced, while the organization of APGs in the same conditions is not always possible. This can be explained by the fact that the streamer discharge is not sensitive to the secondary electron emission from the dielectric surface while it is critical for the operation of APGs.

It is an established fact that the glow discharge will go through a contraction phase with increase of pressure due to thermionic instability. Because of instabilities, the glow discharge is usually produced at low pressures (about 1 Torr). In the case of APGs the effect of thermionic instability is reduced by using an alternating voltage; thus, the discharge operates only when the voltage is high enough to satisfy the Townsend criteria, and the rest of the time the discharge is idle. This idle operation phase allows time for heat and active species dissipation. If the time between excitation cycles is not enough for the dissipation then instability will develop and the discharge will undergo transition to a filamentary mode. Transition from an APG to a filamentary mode with increasing frequency was observed experimentally [74].

It is interesting to note that in the case of an APG discharge, avalanche to streamer transition will depend on the pre-ionization level in the discharge. The Meek condition was derived for an isolated avalanche. In the case of a high pre-ionization level, avalanches will be produced close to each other and will electrostatically affect each other. Such electrostatic interaction between avalanches will depend on the distance between them. If two avalanches develop close enough to each other then the transition to a streamer can be prevented and the discharge will remain uniform. In order to derive the modified Meek condition, let us assume that two avalanches separated by a distance  $L$  start simultaneously ( $R$  is the radius of the avalanche at the time it reaches the anode). The electric field will be the superposition of the electric fields produced by the two avalanches:

$$E = \frac{1}{4\pi\epsilon_0} \left( \frac{Q}{R^2} - \frac{Q}{(L-R)^2} \right) = \frac{Q}{4\pi\epsilon_0 R^2} \times \left( \frac{1 - 2(R/L)}{(1 - R/L)^2} \right) = E_0 \left( 1 - \frac{R^2}{(L-R)^2} \right). \quad (39)$$

In this equation,  $E_0$  is the electric field produced by one avalanche as it appears in the original Meek derivation [35]. By repeating the original Meek derivation with a modified electric field one can get the condition for avalanche to streamer transition in condition scenarios when avalanches cannot be considered as isolated.

$$\frac{1 - 2(R/L)}{(1 - R/L)^2} \approx 1 - \left( \frac{R}{L} \right)^2, \quad (40)$$

$$\alpha d - \left( \frac{R}{L} \right)^2 \approx \text{const}, \quad (41)$$

$$\alpha d \approx \text{const} + n_e R^2 d. \quad (42)$$

In equation (42), the average distance between avalanches is approximated using pre-ionization concentration. The constants in equations (41) and (42) depend on the operational gas; for example, in air at 1 atm this constant equals 20. The modified Meek criterion suggests that the avalanche to streamer transition can be avoided by increasing the avalanche radius and by providing sufficient pre-ionization.

The operational gas plays a very important role in the transition to APG mode. For example, helium has very high electronic excitation levels and no electron energy losses on vibrational excitation, resulting in high values of electron temperatures at lower levels of the reduced electric field. Also, fast heat and mass transfer processes in helium prevent contraction and other instability effects in the glow discharge at high pressures. The same processes can be important in preventing the generation of space-localized streamers and sparks. More details regarding the APG discharges can be found in [36–38].

### 5.7. Ferroelectric discharges

Special properties of DBDs of practical interest can be revealed by using ferroelectric ceramic materials of high dielectric permittivity ( $\epsilon > 1000$ ) as dielectric barriers [39]. Today, ceramics based on  $\text{BaTiO}_3$  are the most widely employed ferroelectric material for DBDs.

Important physical peculiarities of the ferroelectric discharges are related to the physical nature of the ferroelectric materials, which can be spontaneously polarized in a given temperature interval. Such spontaneous polarization means that the ferroelectric materials can have a non-zero dipole moment even in the absence of an external electric field. The electric discharge phenomena accompanying contact of a gas with a ferroelectric sample were first observed in detail by Robertson and Baily [40], and the first qualitative description of this sophisticated phenomenon was given by Kusz [41].

The long-range correlated orientation of dipole moments can be destroyed in ferroelectrics by thermal motion. The temperature at which the spontaneous polarization vanishes is called the temperature of ferroelectric phase transition or the ferroelectric Curie point. When the temperature is below the ferroelectric Curie point, the ferroelectric sample is divided into macroscopic uniformly polarized zones called the ferroelectric domains.

The directions of the polarization vectors of individual domains in the equilibrium state are set up in such a way that the internal energy of the crystal is minimized and the polarization of the sample as a whole is close to zero. Application of an external AC voltage leads to overpolarization of the ferroelectric material and reveals strong local electric fields on the surface. As was shown in [42], these local surface electric fields can exceed  $10^6 \text{ V cm}^{-1}$ , which stimulate the discharge on ferroelectric surfaces.

The active volume of the ferroelectric discharge is located in the vicinity of the dielectric barrier, which is essentially the narrow interelectrode gap typical for the discharge. Thus, the scaling of the ferroelectric discharge can be achieved by using some special configurations. One such special discharge configuration comprises a series of parallel, thin ceramic plates. High dielectric permittivity of ferroelectric ceramics enables such multi-layer sandwiches to be supplied by only two edge electrodes. Another interesting configuration can be obtained by using a packed bed of ferroelectric pellets. In the same manner non-equilibrium plasma is created in such a system in the void between the pellets.

### 5.8. The gliding arc discharges

Conventional thermal and non-thermal discharges cannot provide simultaneously a high level of non-equilibrium, and high electron temperature and high electron density, whereas most prospective plasma-chemical applications require both: a high power for efficient reactor productivity and a high degree of non-equilibrium to support chemical processes selectively. That is why one of the vital challenges of modern plasma chemistry is to unite the advantages of thermal and non-thermal plasma systems by developing powerful and high-pressure discharges, generating non-equilibrium cold plasma, which can be applied, in particular, for large scale exhaust gas cleaning, pollution control, fuel conversion, hydrogen production and surface treatment.

One of the possible ways of creating such a hybrid plasma is to use the transient type of arc—the gliding arc (GA) discharge [43–45]. This periodic discharge evolves during a cycle from arc to a strongly non-equilibrium discharge, with still relatively high levels of electron density. Because of

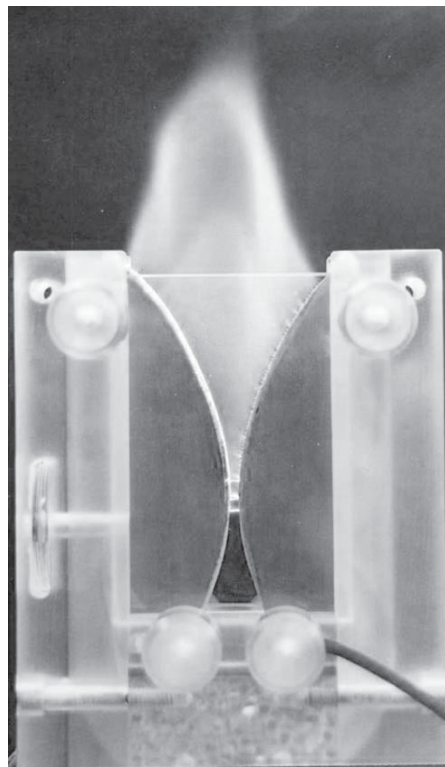


**Figure 20.** Photo image of the GA in the parallel flow reactor.

this, the non-equilibrium GA is very effective for the above-mentioned applications. The non-equilibrium GA is a very sophisticated physical phenomenon: this transitional quasi-equilibrium/non-equilibrium discharge is essentially non-uniform in time and in space, and includes ‘mysterious’ internal transition from thermal to non-thermal mechanisms of ionization.

The GA discharge is organized in a gas flow between two divergent electrodes (see figure 20) and starts at the shortest distance between the electrodes, then moves with the gas flow at a velocity of about  $10 \text{ m s}^{-1}$  and the length of the arc column increases together with the voltage. When the length of the GA exceeds its critical value  $l_{\text{crit}}$ , heat losses from the plasma column begin to exceed the energy supplied by the source, and it is not possible to sustain the plasma in a state of thermodynamic equilibrium. As a result, a fast transition into a non-equilibrium phase occurs. The discharge plasma cools rapidly to gas temperature and the plasma conductivity is maintained by a high value of the electron temperature  $T_e \sim 1 \text{ eV}$ . After this fast transition, the GA continues its evolution, but under non-equilibrium conditions ( $T_e \gg T_{\text{gas}}$ ). The specific heat losses in this regime are much smaller than in the equilibrium regime (numerically about three times less). The discharge length increases up to a new critical value  $l \cong 3l_{\text{crit}}$ . The main part of the GA power (up to 75–80%) can be dissipated in the non-equilibrium zone. After the decay of the non-equilibrium discharge, the evolution repeats from the initial breakdown. This permits the stimulation of chemical reactions in regimes quite different from conventional combustion and environmental situations.

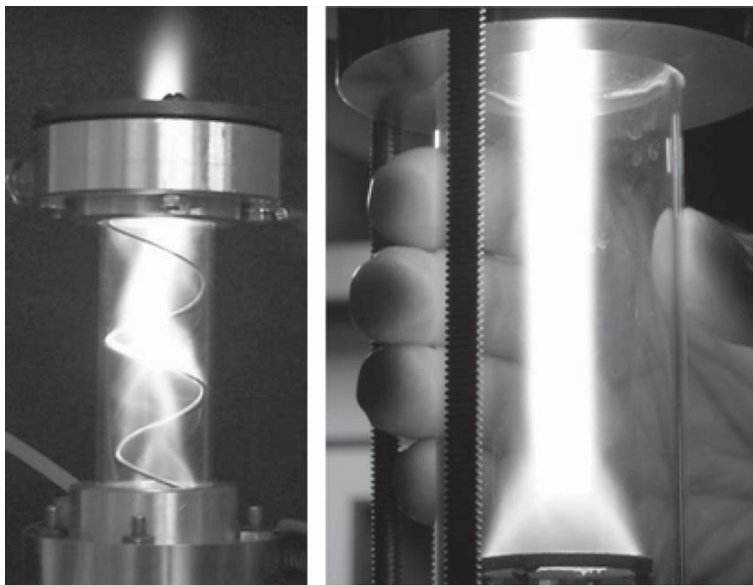


**Figure 21.** Photo images of the low current GA in Tornado reactors.

Recent research into and development of the GA demonstrated that GA can exist in two different regimes: the high-current GA (HCGA, with current  $I \geq 10$  A), which starts as an equilibrium discharge and transforms into a non-equilibrium one at the end of the cycle during the plasma decay; and the low-current GA (LCGA,  $I \leq 1$  A), which is non-equilibrium during the whole cycle of evolution. HCGA can be generally considered as a conventional thermal arc with strong convective cooling by a fast transversal gas flow and with specific boundary conditions on the electrodes. As the conventional thermal arcs are studied very well, the analysis of the HCGA is relatively simple at all stages of evolution except the last one—fast equilibrium/non-equilibrium transition (FENETRe) during the elongated plasma decay.

LCGA is very promising for different plasma chemical applications since it can provide a high degree of non-equilibrium to support chemical reactions selectively. An especially promising method is to use LCGA in reverse vortex geometry—‘Tornado’ flow (see figure 21). Reverse vortex flows [46–50] provide excellent insulation of active species generated by the plasma from the apparatus walls. Also, it is very important that the residence time of the plasma gas in the Tornado apparatus is relatively high in spite of very high circumferential velocity, which is necessary for intensive cooling of GA. So, this property provides the ability to increase specific power input and ensure uniform treatment of plasma gas that is impossible to realize in another GA system.

The GA discharge was first used in chemical applications in the nineteenth century for the production of nitrogen-based fertilizers [51]. It became popular again in the early 1990s [43, 44]. Recent applications involve gas conversion processes [52], such as carbon dioxide [53, 54] or steam [55, 55] reforming of methane to produce synthesis gas ( $\text{CO} + \text{H}_2$ ); oxidation of low concentration  $\text{H}_2\text{S}$  into  $\text{SO}_2$  for pollution control [57, 58]; and VOC treatment for environmental protection [59–61]. The GAs can be arranged, depending on current and flow rate, as completely thermal

(at high currents), completely non-thermal (lowest currents), and as a transitional discharge (at intermediate currents) [62]. The transitional regime is the most practical one because it is mainly non-thermal though still powerful and remembering its ‘quasi-thermal past’ (‘the memory effect’) [62]. Former phenomenological models [44, 45, 63] claimed FENETRe in a narrow window between quasi-thermal and non-thermal phases of the transitional GA.

Although some success in practical application has already been achieved, wide-ranging application of this discharge requires a deeper understanding of its physics and chemistry, particularly of the heat/mass transfer in the transitional regime.

## 6. Spark discharges

### 6.1. Development of a spark channel, back wave of strong electric field and ionization

When streamers provide an electrical connection between electrodes and neither a pulse power supply nor a dielectric barrier prevents further growth of current, it opens up the opportunity for development of a spark. However, the initial streamer channel does not have a very high conductivity and usually provides only a very low current of about 10 mA. Thus, some fast ionization phenomenon takes place after formation of an initial streamer channel to increase the degree of ionization, the current and to an intense spark.

The potential of the head of the cathode-directed streamer is close to the anode potential. This is the region of strong electric field around the streamer’s head. While the streamer approaches the cathode, this electric field is obviously growing. It stimulates intense formation of electrons on the cathode surface and its vicinity and subsequently their fast multiplication in this elevated electric field. New ionization waves much more intense than the original streamer now start propagating along the streamer channel but in the opposite

direction from the cathode to the anode. This is usually referred to as the back ionization wave, and propagates back to the anode with an extremely high velocity of about  $10^9 \text{ cm s}^{-1}$ .

The high velocity of the back ionization wave is not directly the velocity of electron motion, but rather the phase velocity of the ionization wave. The back wave is accompanied by a front of intensive ionization and the formation of a plasma channel with sufficiently high conductivity to form a channel of the intensive spark.

The radius of the spark channel grows to about 1 cm, which corresponds to a spark current increase of  $10^4$ – $10^5$  A, at current densities of about  $10^4 \text{ A cm}^{-2}$ . The plasma conductivity becomes relatively high and a cathode spot can be formed on the electrode surface. The interelectrode voltage decreases to a value lower than the initial one, and the electric field becomes about  $100 \text{ V cm}^{-1}$ . If voltage is supplied by a capacitor, the spark current obviously starts decreasing after reaching the maximum values mentioned.

The detailed theory of the electric sparks was developed by Drabkina [64] and Braginsky [65]; extensive modern experimental and simulation material on the subject can be found in a book of Baselyan and Raizer [32].

### 6.2. Laser directed spark discharges

Modification of sparks can be done by synergetic application of high voltages with laser pulses [66, 67]. It is interesting that laser beams can direct spark discharges not only along straight lines but also along more complicated trajectories. Laser radiation is able to stabilize and direct the spark discharge channel in space through one of three major effects: local preheating of the channel, local photoionization and optical breakdown of gas.

Preheating of the discharge channel creates a low gas density zone, leading to higher levels of reduced electric field, which is favourable, as a result, for spark propagation. This effect works best if special additives provide the required absorption of the laser radiation. For example, if a  $\text{CO}_2$ -laser is used for preheating, a strong effect on the corona discharge can be achieved when about 15% ammonia (which effectively absorbs radiation at a wavelength of  $10.6 \mu\text{m}$ ) is added to air. At a laser radiation density of about  $30 \text{ J cm}^{-2}$ , the breakdown voltage in the presence of ammonia decreases by an order of magnitude. The maximum length of the laser-supported spark in these experiments was 1.5 m. Effective stabilization and direction of the spark discharges by a  $\text{CO}_2$  laser in air was also achieved by admixtures of  $\text{C}_2\text{H}_2$ ,  $\text{CH}_3\text{OH}$  and  $\text{CH}_2\text{CHCN}$ .

Photoionization by laser radiation is able to stabilize and direct a corona discharge without significantly changing the gas density by means of local pre-ionization of the discharge channel. UV-laser radiation (e.g. Nd-laser or KrF-laser) should be applied in this case. Ionization is usually related to the two-step photoionization process of special organic additives with relatively low ionization potential. The UV KrF-laser with pulse energies of approximately 10 mJ and pulse duration of approximately 20 ns is able to stimulate the directed spark discharge to lengths of 60 cm. Note that the laser photoionization effect to stabilize and direct sparks is limited in air by fast electron attachment to oxygen molecules. In this case, photo-detachment of electrons from negative ions can be

provided by using a second laser radiating in the infrared or visible range.

The most intense laser effect on spark generation can be provided by the optical breakdown of the gases. The length of such a laser spark can exceed 10 m. The laser spark in pure air requires a power density of the Nd laser ( $\lambda = 1.06 \mu\text{m}$ ) exceeding  $10^{11} \text{ W cm}^{-2}$ .

## 7. Conclusion

In this paper, we discussed the physics of breakdown phenomena and the most common non-thermal atmospheric pressure plasma discharges. However, in order to apply non-equilibrium plasma technology to particular applications, a number of challenging engineering problems should be addressed. For example, in plasma display panels that use DBD systems there is a need for better understanding of the basic physical phenomena in order to improve efficiency and the definition, addressing speed and contrast [68]. Another challenge that faces many researchers is a low specific power of nonequilibrium discharges. In many applications it is desirable to have a high power density in order to increase product yield. In the search for ideas, several types of hybrid discharges were introduced. One of the most interesting examples of such a hybrid discharge is the GA discharge. The GA starts as a thermal discharge and then a transition into non-equilibrium condition occurs. That is why this discharge combines the power of the thermal discharge with the selectivity of a non-equilibrium plasma.

Non-uniformity in space and time as well as strong thermodynamic non-equilibrium are distinctive properties of non-thermal discharges, which allow us to hope for an expansion of its applications in low temperature atmospheric pressure plasma chemistry. Non-thermal discharges have much potential as a prospective technology for exhaust gas cleaning from  $\text{CO}_2$ ,  $\text{NO}_x$  and VOCs, especially after recent pioneering research work in this direction gave very promising results. Applications of non-thermal plasmas in problems of cleaning, etching and surface modification are within reach.

## References

- [1] Raizer Yu P 1991 *Gas Discharge Physics* (Berlin: Springer)
- [2] Raether H 1964 *Electron Avalanches and Breakdown in Gases* (London: Butterworth)
- [3] Loeb L B 1960 *Basic Processes of Gaseous Electronics* (Berkeley, CA: University of California Press)
- [4] Meek J M and Craggs J D 1978 *Electrical Breakdown of Gases* (New York: Wiley)
- [5] Lozansky E D and Firsov O B 1975 *Theory of Sparks* (Moscow: Atomizdat)
- [6] Dawson G A and Winn W P 1965 *Z. Phys.* **183** 159
- [7] Gallimberti I 1972 *J. Phys. D: Appl. Phys.* **5** 2179
- [8] Klingbeil R D, Tidman A and Fernsler R F 1972 *Phys. Fluids* **15** 1969
- [9] Baselyan E M and Goryunov A Yu 1986 *Electrichestvo (J. Electricity)* **11** 27
- [10] Gallimberti I 1977 *Electra* **76** 5799
- [11] Loeb L B 1965 *Electrical Coronas—Their Basic Physical Mechanisms* (Berkeley, CA: University of California Press)
- [12] Goldman M and Goldman N 1978 *Gaseous Electronics* ed M N Hirsh and H J Oscam (New York: Academic)
- [13] Roth J R 2000 *Industrial Plasma Engineering* (Bristol: Institute of Physics Publishing)

- [14] Mattachini F, Sani E and Trebbi G 1996 *Proc. Int. Workshop on Plasma Technologies for Pollution Control and Waste Treatment* (Cambridge, MA: MIT Press)
- [15] Pu Y K and Woskov P P 1996 *Proc. Int. Workshop on Plasma Technologies for Pollution Control and Waste Treatment* (Cambridge, MA: MIT Press)
- [16] Mattachini F, Sani E and Trebbi G 1996 *Proc. Int. Workshop on Plasma Technologies for Pollution Control and Waste Treatment* (Cambridge, MA: MIT Press)
- [17] Penetrante B M, Brusasco R M, Meritt B T, Pitz W J, Vogtlin G E, Kung M C, Kung H H, Wan C Z and Voss K E 1998 *Plasma Exhaust Aftertreatment* (Warrendale, PA: Society of Automotive Engineers)
- [18] Korobtsev S, Medvedev D, Rusanov V and Shiryayevsky V 1997 *13th Int. Symp. on Plasma Chemistry (Beijing, China)* vol 2, p 755
- [19] Park M, Chang D, Woo M, Nam G and Lee S 1998 *Plasma Exhaust Aftertreatment* (Warrendale, PA: Society of Automotive Engineers)
- [20] Sobacchi M G, Saveliev A V, Fridman A A and Kennedy L A 2002 *Int. J. Hydrogen Energy* **27** 635–42
- [21] Kogelschatz U, Eliasson B and Egli W 1997 *J. Physique IV (Colloque)* **7** 4–47
- [22] Siemens W 1857 *Poggendorfs Ann. Phys. Chem.* **102** 66
- [23] Klemenc A, Hinterberger H and Hofer H 1937 *Z. Elektrochem.* **43** 261
- [24] Kogelschatz U 1988 *Process Technologies for Water Treatment* ed S Stucki (New York: Plenum) pp 87–120
- [25] Kunchardt E E and Tzeng Y 1988 *Phys. Rev. A* **38** 1410
- [26] Djermoune D, Samson S, Marode E and Segur P 1995 *11th Int. Conf. on Gas Discharges and their Applications (Tokyo)* vol 2, pp 484–7
- [27] Kulikovskiy A A 1994 *J. Phys. D: Appl. Phys.* **27** 2556
- [28] Babaeba N and Naidis G 1996 *J. Phys. D: Appl. Phys.* **29** 2423
- [29] Vitello P A, Penetrante B M and Bardsley J N 1994 *Phys. Rev. E* **49** 5574
- [30] Xu X P and Kushner M J 1998 *J. Appl. Phys.* **84** 4153
- [31] [Chirokov A, Gutsol A, Fridman A, Sieber K D, Grace J M and Robinson K S 2004 Analysis of two-dimensional microdischarge distribution in dielectric-barrier discharges \*Plasma Sources Sci. Technol.\* \*\*13\*\* 623–35](#)
- [32] Baselyan E M and Raizer Yu P 1997 *Spark Discharge* (Moscow: Moscow Institute of Physics and Technology)
- [33] Heath W O and Birmingham J G 1995 *Annual Meeting of American Nuclear Society PNL-SA-25844 Pacific Northwest Laboratory, Philadelphia, PA*
- [34] Birmingham J G and Moore R R 1990 Reactive bed plasma air purification *United States Patent* # 4,954,320
- [35] Meek J M 1940 *Phys. Rev.* **57** 722
- [36] Kanazawa S, Kogoma M, Moriwaki T and Okazaki S 1988 *J. Phys. D: Appl. Phys.* **21** 838
- [37] Lacour B and Vannier C 1987 *J. Appl. Phys.* **38** 5244
- [38] Honda Y, Tochikubo F and Watanabe T 2001 *25th Int. Conf. on Phenomena in Ionized Gases ICPIG-25 (Nagoya, Japan)* vol 4, p 37
- [39] Opalinska T and Szymanski A 1996 *Contrib. Plasma Phys.* **36** 63
- [40] Robertson G D and Baily N A 1965 *Bull. Am. Phys. Soc.* **2** 709
- [41] Kusz J 1978 *Plasma Generation on Ferroelectric Surface* (Warsaw-Wroclaw: PWN)
- [42] Hinazumi H, Hosoya M and Mitsui T 1973 *J. Phys. D: Appl. Phys.* **21** 1973
- [43] Czernichowski A 1994 *Pure Appl. Chem.* **66** 1301
- [44] Fridman A, Czernichowski A, Chapelle J, Cormier J M, Lesueur H and Stevefelt J 1994 *J. Phys.* **4** 1449
- [45] Fridman A, Nester S, Kennedy L A, Saveliev A V and Mutaf-Yardimci O 1999 *Prog. Energy Combust. Sci.* **25** 211
- [46] Kalinnikov V T and Gutsol A F 1997 *Sov. Phys.—Dokl.* **42** 179
- [47] Gutsol A and Bakken J A 1998 *J. Phys. D: Appl. Phys.* **31** 704
- [48] Gutsol A, Larjo J and Hernberg R 2002 *Plasma Chem. Plasma Process.* **22** 351
- [49] Chirokov A, Gutsol A, Fridman A and Kennedy L 2001 *15th Int. Symp. on Plasma Chemistry (Orleans, 9–13 July)* vol 1, p 167
- [50] Kalra C S, Kossitsyn M, Iskenderova K, Chirokov A, Cho Y I, Gutsol A and Fridman A 2003 *Electron. Proc. 16th Int. Symp. on Plasma Chemistry (Taormina, Italy, 22–27 June)* ISPC-565
- [51] Naville A A and Guye C E 1904 *French Patent* 350 120
- [52] Wendt A and Heberlein J V 1995 *Low Pressure Non-equilibrium Plasma Applications, Proc. Workshop on Industrial Applications of Plasma Chemistry (25–26 August) (Minneapolis, MN)* vol A
- Smith R and Heberlein J V 1995 *Thermal Plasma Applications Proc. Workshop on Industrial Applications of Plasma Chemistry (25–26 August) (Minneapolis, MN)* vol B
- [53] Lesueur H, Czernichowski A and Chapelle J 1994 *Int. J. Hydrogen Energy* **19** 139
- [54] Iskenderova K, Porshnev P, Gutsol A, Saveliev A, Fridman A, Kennedy L and Rufael T 2001 *15th Int. Symp. on Plasma Chemistry (Orleans)* vol VII, p 2849
- [55] Meguernes K, Czernichowski A and Chapelle J 1995 *VDI-Berichte* **1166** 495
- [56] Czernichowski A and Meguernes K 1995 *12th Int. Symp. on Plasma Chemistry (Minneapolis, MN)* vol 2, p 729
- [57] Czernichowski A and Lesueur R A 1992 *Proc. NATO Advanced Research Workshop on Thermal Plasma Techniques for Pollution Control* vol 61 (Cambridge: Cambridge University Press)
- [58] Dalaine V, Cormier J M and Lefauchaux P 1998 *J. Appl. Phys.* **83** 2435
- [59] Fridman A, Sobacchi M, Saveliev A, Gutsol A and Kennedy L A 2001 *199th Meeting of the Electrochemical Society (Washington)* vol 2001-1 Abstract no 196
- [60] Sobacchi M, Saveliev A, Fridman A, Gutsol A and Kennedy L 2001 *15th Int. Symp. on Plasma Chemistry (Orleans)* vol VII, p 3135
- [61] Kalashnikov N 2002 Non-equilibrium gliding arc and corona discharges for abatement of volatile organic compounds *PhD Thesis* UIC, Chicago, IL
- [62] Mutaf-Yardimci O, Saveliev A, Fridman A and Kennedy L 2000 *J. Appl. Phys.* **87** 1632
- [63] Rusanov V D, Liventsov V V, Potapkin B V, Fridman A, Czernichowski A and Chapelle J 1995 *Sov. Phys.—Dokl.* **40** 623
- [64] Drabkina S I 1951 *Sov. Phys.—JETP* **21** 473
- [65] Braginsky S I 1958 *Sov. Phys.—JETP* **34** 1548
- [66] Vasilyak L M, Kostuchenko S V, Kurdyavtsev N N and Filugin I V 1994 *Adv. Phys. Sci. (Usp. Fiz. Nauk)* **164** 263
- [67] Asinovsky E I and Vasilyak L M 2001 *Encyclopedia of Low Temperature Plasma* vol 2, ed V E Fortov (Moscow: Nauka (Science)) p 234
- [68] [Boeuf J P 2003 Plasma display panels: physics, recent developments and key issues \*J. Phys. D: Appl. Phys.\* \*\*36\*\* R53](#)
- [69] Lowke J J and D'Alessandro F 2003 *J. Phys. D: Appl. Phys.* **36** 2673
- [70] Hood J L 1980 *Int. Conf. on Gas Discharges and Their Applications (Edinburgh)* p 86
- [71] Uehara T 1999 *Adhesion Promotion Techniques* (New York: Dekker)
- [72] Penetrante B M, Brusasco R M, Merritt B T and Vogtlin G E 1999 *Pure Appl. Chem.* **71** 1829
- [73] Rosocha L A, Platts D, Coates D M and Stange S 2004 *Proc. 1st Int. Workshop on Plasma-Assisted Combustion (PAC) (Albuquerque, NM)*
- [74] Croquesel E, Gherardi N, Martin S and Massines F 2000 *Proc. HAKONE VII 7th Int. Symp. on High Pressure Low Temperature Plasma Chemistry (Greifswald)* vol 1, p 88
- [75] Massines F and Gouda G 1998 *J. Phys. D: Appl. Phys.* **31** 3411
- [76] Fortov V E 2002 *Encyclopedia of Low Temperature Plasma* (Moscow: Nauka (Science))
- [77] Chyin V I 2002 *Phys. Condens. Matter* **5** 429